

# Probing local nonlinear viscoelastic properties in soft materials

S. Chockalingam<sup>a</sup>, C. Roth<sup>b,c</sup>, T. Henzel<sup>b</sup>, T. Cohen<sup>b,d,\*</sup>

<sup>a</sup>*Massachusetts Institute of Technology, Department of Aeronautics and Astronautics, Cambridge, MA, 02139, USA*

<sup>b</sup>*Massachusetts Institute of Technology, Department of Civil and Environmental Engineering, Cambridge, MA, 02139, USA*

<sup>c</sup>*École Polytechnique Fédérale de Lausanne (EPFL), Institute of Mechanical Engineering, 1015 Lausanne, Switzerland*

<sup>d</sup>*Massachusetts Institute of Technology, Department of Mechanical Engineering, Cambridge, MA, 02139, USA*

---

## Abstract

Minimally invasive experimental methods that can measure local rate dependent mechanical properties are essential in understanding the behaviour of soft and biological materials in a wide range of applications. Needle based measurement techniques such as Cavitation Rheology (Zimberlin et al., 2007) and Volume Controlled Cavity Expansion (VCCE, Raayai-Ardakani et al. (2019a)), allow for minimally invasive local mechanical testing, but have been limited to measuring the elastic material properties. Here, we propose several enhancements to the VCCE technique to adapt it for characterization of viscoelastic response at low to medium stretch rates ( $10^{-2}$  -  $1\text{ s}^{-1}$ ). Through a carefully designed loading protocol, the proposed technique performs several cycles of expansion-relaxation at controlled stretch rates in a cavity expansion setting and then employs a large deformation viscoelastic model to capture the measured material response. Application of the technique to soft PDMS rubber reveals significant rate dependent material response with high precision and repeatability, while isolating equilibrated states that are used to directly infer the quasistatic elastic modulus. The technique is further established by demonstrating its ability to capture changes in the rate dependent material response of a tuneable PDMS system. The measured viscoelastic properties of soft PDMS samples are used to explain earlier reports of rate insensitive material response by needle based methods: it is demonstrated that the conventional use of constant volumetric rate cavity expansion can induce high stretch rates that lead to viscoelastic stiffening and an illusion of rate insensitive material response. We thus conclude with a cautionary note on possible overestimation of the quasistatic elastic modulus in previous studies and suggest that the stretch rate controlled expansion protocol, proposed in this work, is essential for accurate estimation of both quasistatic and dynamic material parameters.

*Keywords:* Viscoelasticity, Soft materials, Volume controlled cavity expansion, Rate dependent effects

---

\*Corresponding author: talco@mit.edu

## 1. Introduction

Mechanical characterisation of soft and biological materials is important in several applications including tissue engineering (Engler et al., 2004; Kong et al., 2005; Vedadghavami et al., 2017), food science (Finney, 1967; Solomon and Jindal, 2007), disease detection (Yeh et al., 2002; Paszek et al., 2005; Samani and Plewes, 2007; Last et al., 2011) and study of biological processes such as growth and morphogenesis (Budday et al., 2014; von Streng et al., 2020). Biological tissues are often heterogeneous and their mechanical properties can change significantly when removed from their native environment (Nickerson et al., 2008). Experimental techniques that can measure the mechanical properties of biological materials both locally and *in vivo* are thus essential for accurate characterisation of the material response. For this reason, the Cavitation Rheology technique has emerged as a popular choice for estimation of local elastic material properties of soft and biological materials (Zimberlin et al., 2010; Zimberlin and Crosby, 2010; Cui et al., 2011; Crosby and McManus, 2011; Delbos et al., 2012; Chin et al., 2013; Blumlein et al., 2017; Fuentes-Caparrós et al., 2019; Polio et al., 2018; Zilonova et al., 2018). In this method, by pressure-controlled inflation, a cavity is expanded in the material at the tip of a needle. Through this inflation process, the pressure inside the cavity reaches a maximum that is assumed to correspond to the theoretically predicted elastic cavitation instability limit, which is used to determine the elastic modulus. Despite its success, the Cavitation Rheology technique often results in fracture of the sample prior to reaching the cavitation instability limit and relies on an *a priori* assumption on the constitutive response. The Volume Controlled Cavity Expansion (VCCE) technique (Raayai-Ardakani et al., 2019a; Raayai-Ardakani and Cohen, 2019) remedies these problems by performing a volume controlled expansion of the cavity using injection of an incompressible fluid and then using the pressure volume data (prior to fracture) to extract the nonlinear elastic material properties, as recently demonstrated in application for characterising brain tissue response (Mijailovic et al., 2020).

While application of needle based techniques has been demonstrated for the measurement of rate independent properties, soft and biological materials often exhibit viscoelastic response, which plays a role in several applications such as disease detection (Streitberger et al., 2011; Tram and Swindle-Reilly, 2018), study of adhesion behaviour (Castellanos et al., 2011; Prowse et al., 2011; Reza et al., 2014), understanding tissue response when subjected to high-intensity focused ultrasound (Zilonova et al., 2018), and study of skin pain sensation (Liu et al., 2015). These applications emphasize the need for reliable experimental techniques that can extract the local nonlinear viscoelastic material properties for soft and biological materials. However, conventional viscoelastic testing methods suffer from several drawbacks when it comes to testing of such materials. For example, uniaxial and simple shear viscoelastic testing (Mao et al., 2017; Budday et al., 2017) of soft materials need to overcome several challenges: sample preparation in specific shapes, boundary effects, and inhomogeneous deformation (Rashid et al., 2012; Budday et al., 2017). Moreover, for testing of biological tissues, they require the specimen to be cut and taken out of its native environment, negating the possibility of *in vivo* testing. Additionally, only bulk properties of the tissues can be extracted which is not ideal for mechanical characterisation of biological materials that are usually heterogeneous. Alternatively, small-scale indentation based techniques allow for local viscoelastic material testing (Balooch et al., 1998; Zheng and Mak, 1999; Mahaffy et al., 2004; VanLandingham et al., 2005; Hu et al., 2010; Budday et al., 2015). However, accurate determination of material properties beyond the linear elastic regime

necessitate sophisticated contact mechanics models to be employed which are not always readily available (Lin et al., 2009; Style et al., 2013).

Given the limitations of the conventional testing methods described above, an alternative would be to consider experimental methods for local viscoelastic testing in a cavity expansion setting, as suggested by Cohen and Molinari (2015). Inertial Microcavitation Rheometry (IMR) (Estrada et al., 2018; Yang et al., 2020) is one such recently developed technique that can be used for local viscoelastic material characterisation at ultra-high stretch rates ( $10^3 - 10^8 \text{ s}^{-1}$ ). It uses laser pulses to generate a cavity within the material sample, the ensuing dynamic cavity motion is actively tracked visually and modelled using viscoelastic governing dynamics. The technique is restricted by the requirement of transparent material samples to be able to visually track the cavity motion. Additionally, there is neither an independent measure of the pressure response nor a way to control the stretch rates. Therefore IMR is not a suitable technique for viscoelastic material testing at low to medium stretch rates. Other cavity expansion and instability based techniques such as Cavitation Rheology and VCCE would have to be modified for viscoelastic material testing, as the influence of viscosity can significantly affect both the cavitation instability limit and the pressure response during cavity expansion (Cohen and Molinari, 2015; Kumar et al., 2017).

From the discussion of the strengths and weaknesses of the different experimental techniques above, it is apparent that adapting the VCCE technique for rate dependent testing would provide a promising approach for local and *in vivo* characterisation of nonlinear viscoelastic material response at moderate stretch rates. Thus, in this paper, we propose several modifications to the VCCE technique to adapt it for the viscoelastic characterisation of soft solids at low to medium stretch rates ( $10^{-2} - 1 \text{ s}^{-1}$ ). The modified method performs stretch rate controlled cavity expansion experiments and employs a large deformation nonlinear viscoelastic constitutive model to characterise the experimentally observed material response.

The paper is organized as follows: we begin with some preliminary definitions and an overview of the proposed experimental method in Section 2. This is followed by a detailed description of the experimental technique in Section 3. In Section 4, we present the experimental results for a representative material sample. Then in Section 5, we set up the governing equations and describe the employed large deformation viscoelastic constitutive model. Subsequently in Section 6, the procedure for estimation of the material parameters of the constitutive model from experimental results is described using the representative results from Section 4. The fitted material parameters are used to explain the rate insensitive material response observed in earlier cavity expansion based studies. Finally, in Section 7, we demonstrate the potential of the experimental method by studying the response of PDMS samples with tuneable viscoelasticity. We provide some concluding remarks in Section 8.

## 2. Preliminaries and overview of experimental method

Uniaxial testing methods commonly probe viscoelasticity using stress relaxation experiments wherein the material sample is dynamically elongated and held at a constant stretch. Then, the stress rapidly increases to a peak value followed by relaxation to an equilibrium value over some characteristic timescale. Dynamic unloading of the same sample to a constant stretch causes the stress to rapidly drop, followed by a viscoelastic recovery to an equilibrium value. The proposed experimental method in this paper performs analogous stress relaxation/recovery experiments in

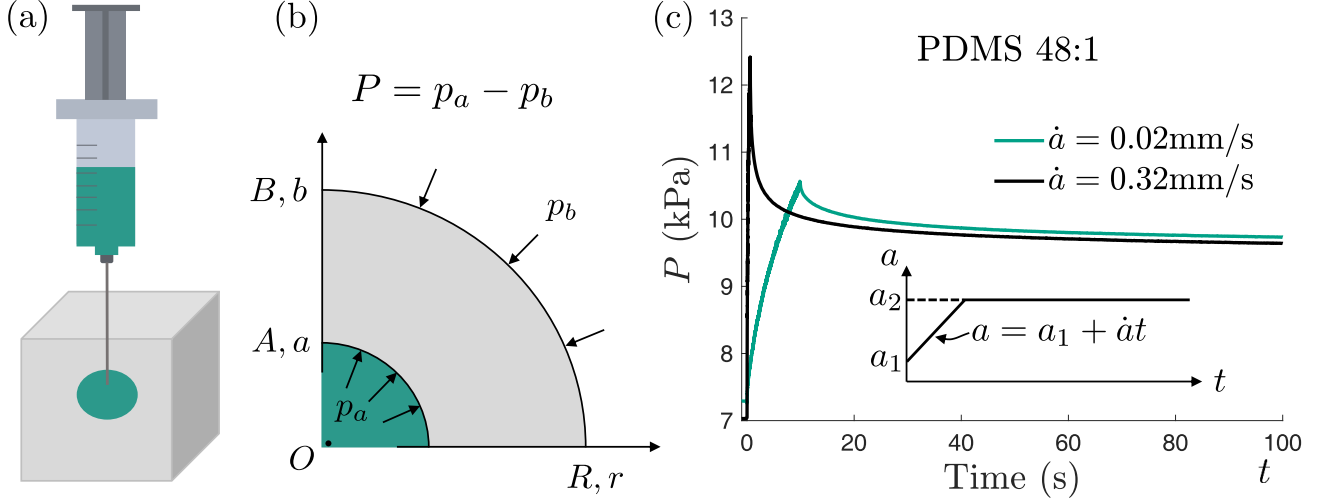


Figure 1: (a) Illustration of Volume Controlled Cavity Expansion inside a soft material sample, through injection of incompressible fluid. (b) Schematic illustration of the cavity expansion problem. The gauge pressure  $P$  is defined as  $P = p_a - p_b$  where  $p_a$  is the pressure applied on the cavity wall and  $p_b = p_{atm}$  is the atmospheric pressure acting on the outer surface of the solid. (c) Rate dependent material response observed in cavity expansion-relaxation experiments for PDMS rubber sample with base:cross-linker ratio of 48:1. The effective cavity size,  $a$ , is increased from a value of  $a_1 = 0.6 \text{ mm}$  at an initial relaxed state to a final size of  $a_2 = 0.8 \text{ mm}$  at a constant cavity expansion rate ( $\dot{a} = \text{const}$ ). Plot of the resulting gauge pressure versus time is shown for two different expansion rates.

the spherical expansion setting of a small cavity.

The experimental method begins with the insertion of a syringe needle into the soft material sample, which creates an initial defect/cavity at the tip of the needle. The cavity is then expanded by performing volume controlled injection of an incompressible and immiscible fluid, as illustrated in Figure 1(a). The pressure inside the cavity is actively measured throughout the experiment. Assuming that the cavity expansion is spherically symmetric, we can define an effective cavity radius,  $a$ , based on the injected volume of fluid  $V$  so that  $a = (3V/4\pi)^{1/3}$ . The effective stress free size of the initial defect is denoted by  $A$  and is retroactively estimated from the pressure-volume data, as later described in Section 6. An effective circumferential stretch at the cavity wall,  $\lambda_a$ , is then defined as  $\lambda_a = a/A$ .

We define the gauge pressure  $P$  as  $P = p_a - p_b$ , where  $p_a$  is the pressure applied on the cavity wall at the interface between the injected fluid and the solid, and  $p_b = p_{atm}$  is the atmospheric pressure acting on the outer surface of the solid. The experimental method prescribes a loading protocol (time profile of specified effective cavity size  $a$ ) that involves several cycles of cavity expansion-relaxation and retraction-recovery between two fixed effective cavity sizes. The resulting experimental gauge pressure profiles are captured using a large deformation nonlinear viscoelastic constitutive model to extract the local viscoelastic material properties.

To motivate the proposed experimental method, we present a precursory experimental result that demonstrates significant viscoelastic effects in the material response of soft PDMS rubber (base:cross-linker ratio of 48:1). The prescribed loading expands an initially relaxed cavity with effective size  $a_1 = 0.6 \text{ mm}$ , to a final size  $a_2 = 0.8 \text{ mm}$ , at a fixed cavity expansion rate ( $\dot{a} = \text{const.}$ ), and then holds the cavity size at  $a_2$  while allowing the material to relax. The resulting experimentally measured gauge pressure is plotted as function of time, for two different cavity

expansion rates, in Figure 1(c). The gauge pressure monotonically increases during expansion to a peak pressure and then relaxes to an equilibrium value when the effective cavity size is held constant. The rate dependence of the material response is apparent from the larger peak pressure for the faster cavity expansion rate and the significant viscoelastic relaxation. The equilibrated pressure which is approximately same for both cavity expansion rates, characterises the equilibrium elastic response of the material.

The successful generation of such experimental pressure curves with accuracy, precision, and repeatability, involves several components including isolation of a fracture-free stretch range, elimination of Mullins effect, and accounting for surface tension effects and dynamic pressure losses. Also important is the identification of a loading protocol that facilitates observation of rate dependent material response while isolating consistent/repeatable equilibrated pressures. These equilibrated pressures are used to extract quasistatic properties of the material whereas the pressure-time curves are used to estimate the dynamic material properties. In the following section, the experimental method is described in detail, including its various individual components that account for the different factors discussed above.

### 3. Experimental method

In the following subsections we describe different aspects of the full experimental protocol which is finally summarised in Table 2.

#### 3.1. Setup

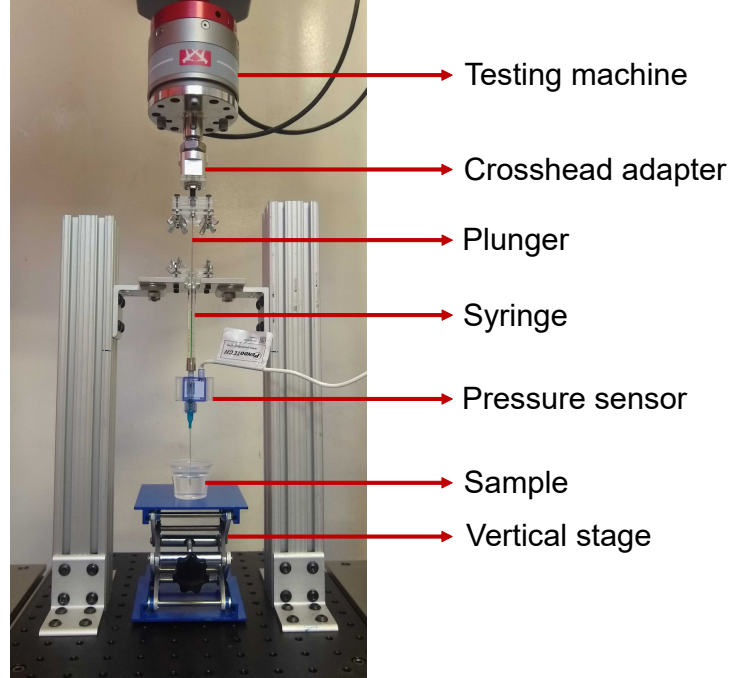


Figure 2: Experimental setup

The experimental setup is shown in Figure 2. It consists of a stationary syringe barrel held by fixed supports and a movable plunger actuated by an Instron® Dynamic Test Instrument. The

syringe is filled with an incompressible fluid (water in this paper) and the plunger displacements control the volume of fluid ejected. An in-line pressure sensor connects to the tip of the syringe and hosts the needle on the other outlet with standard luer connections. The sensor is calibrated using the testing machine as an external transducer. The material sample being studied is placed on a vertical stage and raised until the needle penetrates the material surface. We then perform volume controlled fluid injection and study the dynamic pressure response inside the fluid filled cavity.

A key difference from the VCCE experimental setup in Raayai-Ardakani et al. (2019a) is the measurement of pressure through a pressure sensor rather than through the calibrated forces<sup>1</sup> measured by the testing machine, which results in more reliable and precise pressure measurements. This change also allows the use of a gas-tight high accuracy 50  $\mu\text{L}$  syringe, compared to the 3 mL syringe in Raayai-Ardakani et al. (2019a). The resulting near hundred times reduction in cross sectional area leads to significantly more precise volume control. Use of smaller cross section syringes along with force measurements through the mechanical testing machine is prohibited by unreliable calibration of much higher frictional forces. Hardware components used in the experiment are listed in Table 1.

Table 1: Hardware components including precision where applicable.

Testing machine	Dynamic Instron <sup>®</sup> ElectroPlus <sup>™</sup> E3000 Guaranteed displacement precision: $\pm 0.02$ mm
Syringe	Hamilton <sup>®</sup> Gastight Syringe Model 1705 PTFE Luer (TLL), Capacity 50 $\mu\text{L}$ , surface area $A_s = 0.83$ mm <sup>2</sup> , Max pressure 6.9 MPa = 1000 psi
Needle	Stainless-Steel Dispensing Needles, Blunt Tip Gauge 25 $\mathcal{O}_{out} = 0.51$ mm, $\mathcal{O}_{in} = 0.30$ mm
Pressure Sensor	Pendotech <sup>®</sup> PRESS-S-000, Range: 79 kPa - 520 kPa, Accuracy: $\pm 2\%$ $\forall p < 40$ kPa, Response time 1 ms

### 3.2. Effective cavity size

The effective size of the cavity at any time can be directly calculated from the volume of fluid injected into the material,

$$a = \sqrt{\frac{3}{4\pi} A_s z} \quad (1)$$

where  $z$  is the displacement of the syringe from its initial position. A smaller syringe cross section area  $A_s$  leads to higher accuracy of the measure of  $a$  for given displacement precision of the mechanical testing machine.

<sup>1</sup>Calibration required elimination of frictional forces.

### 3.3. Pressure correction

The raw pressure data measured by the sensor,  $p_m$ , is first corrected by the ambient air pressure  $p_{atm}$ , to obtain the measured gauge pressure  $P_m$ ,

$$P_m = p_m - p_{atm} \quad (2)$$

Although we are interested in measuring the pressure applied on the cavity wall, the pressure

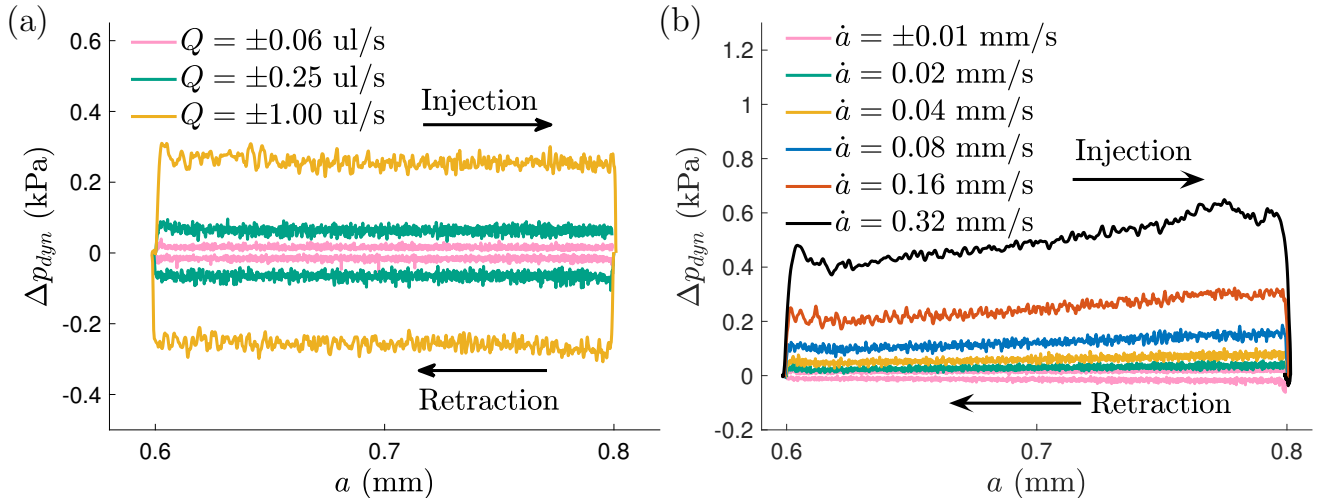


Figure 3: Example experimental calibration curves for dynamic pressure drop correction.

is being measured at some distance from the tip of the needle (Figure 2). While the pressure difference caused due to the weight of the fluid column is negligible for the scale of pressures in our experiments, the dynamic pressure loss caused by the fluid flow in the needle should be accounted for, as well as the possible effect of surface tension. To account for the dynamic pressure loss, we perform calibration experiments by injecting and retracting working fluid from a container at all the different combinations of cavity sizes and expansion rates used in an experiment. Plots of the dynamic drop in pressure ( $\Delta p_{dyn}$ ) from sample calibration experiments are shown in Figure 3, for the cases of constant fluid volume flow rate  $Q$  and constant cavity expansion rate  $\dot{a}$ . It can be seen that the dynamic pressure drop is constant for given flow rate  $Q$  and higher for higher  $Q$ . The drop is non-uniform and increases with  $a$  and  $\dot{a}$  for constant cavity expansion rates (since  $Q = 4\pi a^2 \dot{a}$ ). The gauge pressure inside the fluid in the cavity,  $P_f$ , is then estimated from the measured gauge pressure  $P_m$  as

$$P_f(t) = P_m(t) - \Delta p_{dyn}(a(t), \dot{a}(t)) \quad (3)$$

Calibration for the dynamic pressure correction is performed before every single test. Retraction at even moderate rates can cause detachment between the plunger and the fluid, and thus *we restrict retraction rates to  $\dot{a} > -0.01$  mm/s*. Additionally, at the rates considered here, pressure difference generated due to inertial effects in the fluid container is insignificant. Finally, the gauge pressure at the cavity wall,  $P$ , can be estimated from the gauge pressure inside the fluid

in the cavity,  $P_f$ , by accounting for the effect of surface tension as (Mishra et al., 2018)

$$P(t) = P_f(t) - \frac{2\gamma}{a(t)} \quad (4)$$

where  $\gamma$  is the surface energy for the fluid-solid interface. Henceforth, pressure refers to the cavity wall gauge pressure  $P$ , in eq. (4).

### 3.4. Experiment initiation procedure

To ensure repeatability, in this work we employ a strict protocol to initiate the cavity expansion experiments from a well defined relaxed state. First, the pressure at the tip of the needle is actively monitored as the needle penetrates into the solid by raising the vertical stage (Figure 2). As the solid surface deforms, there is a monotonic increase in pressure, followed by a sudden drop when the surface ruptures. The needle is then slightly retracted, by lowering the stage, to relax most of the compression below the needle ( $p \gtrsim 0$ ) and to ensure that the relaxing material does not block the needle entry. Since the measurement accuracy for small cavity size is unsatisfactory, the cavity is inflated to a size of  $a = 0.5$  mm at a very slow expansion rate of  $\dot{a} < 0.01$  mm/s. In this state, the pressure is given time to relax (1 - 4 hours). For the materials investigated here, cavities formed this way have repeatably proven to be of visually spherical shape and to conserve the spherical geometry during expansion. Hence, this serves as a repeatable well-defined initial condition for all experiments.

### 3.5. Isolating a fracture free stretch range

An important component of the proposed method is the isolation of a cavity stretch range in which the material does not fracture. As discussed in Raayai-Ardakani et al. (2019b), fracture and elastic cavity expansion are intimately coupled. At first when the cavity expands, elasticity dominates the pressure response until a critical pressure  $P_c$  is reached. After this point, the pressure sharply drops as fracture and elastic resistance simultaneously influence the pressure response, as illustrated in Figure 4(a). In this work, we define the cavity stretch range prior to the first sharp pressure drop as fracture free. For the material systems studied here, we observe that  $P_c$  appears to be roughly independent of expansion rate  $\dot{a}$ . A viscoelastic material demonstrates dynamic amplification of elastic resistance, i.e the pressure versus cavity stretch curve steepens compared to the quasistatic limit, as shown in Figure 4(a). This implies that the fracture free cavity stretch range is smaller for higher expansion rates. We experimentally determine the critical effective cavity radius  $a_c$  that initiates fracture at the highest cavity expansion rate we want to probe at. Assuming the effective stress free size of the initial defect,  $A$ , is of similar order between probings,  $a_c$  defines an upper limit of cavity size to be probed to remain fracture free.

### 3.6. Mullins effect

The Mullins effect is often used to describe stress softening after large deformations in soft rubbery materials (Clément et al., 2001; Hanson et al., 2005; Diani et al., 2009). Typically studied for cyclic uniaxial tests (Figure 4(b)), the effect is characterised by a softening behaviour that appears when a stretch value that exceeds values in previous cycles is accessed. Within a previously accessed stretch range, the material responses coincide during the following cycles, aside from a fatigue effect. When the stretch arrives at the maximum value previously applied, the material response reunites with the first uniaxial tension test path.

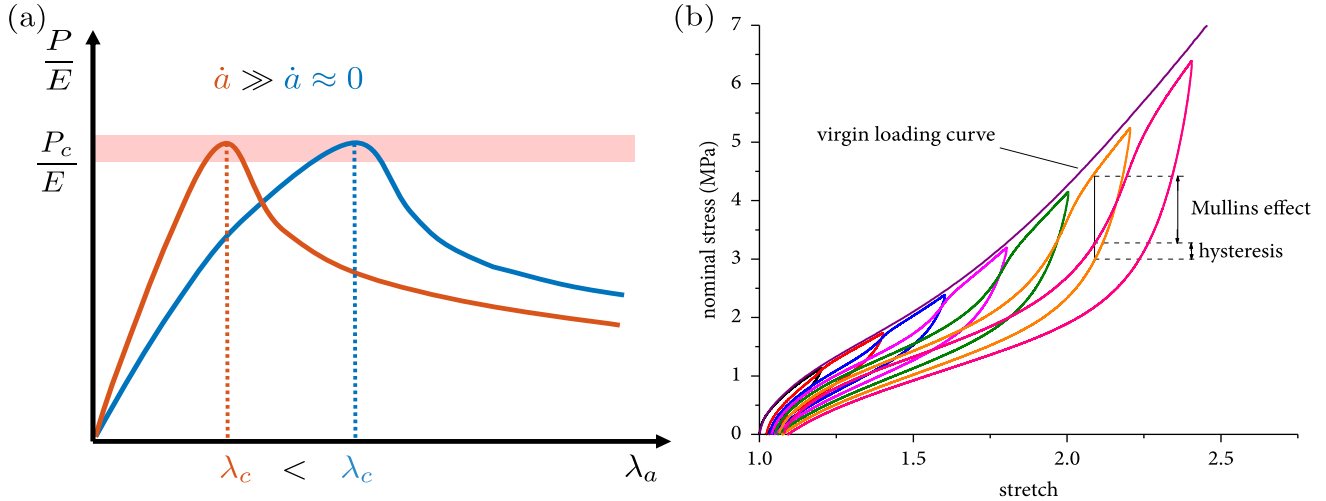


Figure 4: (a) Qualitative illustration of pressure versus cavity stretch before and after onset of fracture, at  $\lambda_c$ . Fracture, identified by a sharp drop in pressure, has been observed to occur at almost the same pressure  $P_c$  for the expansion rates considered here. Increased elastic material resistance at higher expansion rates results in lower values of  $\lambda_c$ . Thus the size of the fracture free cavity stretch range,  $\lambda_a \in [1 \lambda_c]$ , reduces at higher expansion rates. (b) Representative Mullins effect observed in cyclic uniaxial testing of natural/styrene-butadiene (NSBR) rubber (Huang et al., 2019). The different colours correspond to different loading cycles.

We demonstrate the presence of this effect in the cavity expansion setting as well. Starting at a fully relaxed cavity at  $a = 0.5$  mm, fluid is injected at an expansion rate of  $\dot{a} = 0.01$  mm/s up to  $a = 0.5 + \Delta a$  mm. We then immediately retract at a rate of  $\dot{a} = -0.01$  mm/s back to  $a = 0.5$  mm. Three such cycles are performed for increasing values of  $\Delta a$  and before every increase in  $\Delta a$ , the cavity is given time to relax fully. The resulting pressure profiles for a PDMS sample S50-00, whose composition is defined later in Section 7, are shown in Figure 5. The parallels with the Mullins effect for uniaxial cyclic testing in Figure 4 can be clearly seen. For any cycle, a large hysteresis is seen between the expansion and relaxation curves. The expansion pressure profile demonstrates softening on the second cycle for any given  $\Delta a$  but by the third cycle the material responses coincide. The retraction profiles do not demonstrate softening and remain approximately unchanged. In the first cycle ( $n = 1$ ) every time  $\Delta a$  is increased, the pressure profile follows the profile from the previous cycle. *Note the significant change in the pressure whenever  $\dot{a}$  changes sign between expansion and retraction. This is already a clear indicator of viscoelastic rate dependent material response even at this low expansion rate.*

While there is no consensus on the physical source or on the mechanical modeling of Mullins effect (Diani et al., 2009), the present experimental procedure can be applied to obtain further insight into its manifestation in additional stress states (beyond uniaxial tests). However, this is beyond the scope of the present work. Hence, in our experimental protocol, we eliminate the Mullins effect by pre-loading the material in the required stretch range of any experiment and letting the cavity relax at the maximum stretch. To confirm the removal of Mullins effect, we pre-cycle three times in the required experimental range of  $a$  at a very low rate and verify that the hysteresis during expansion is fully removed.

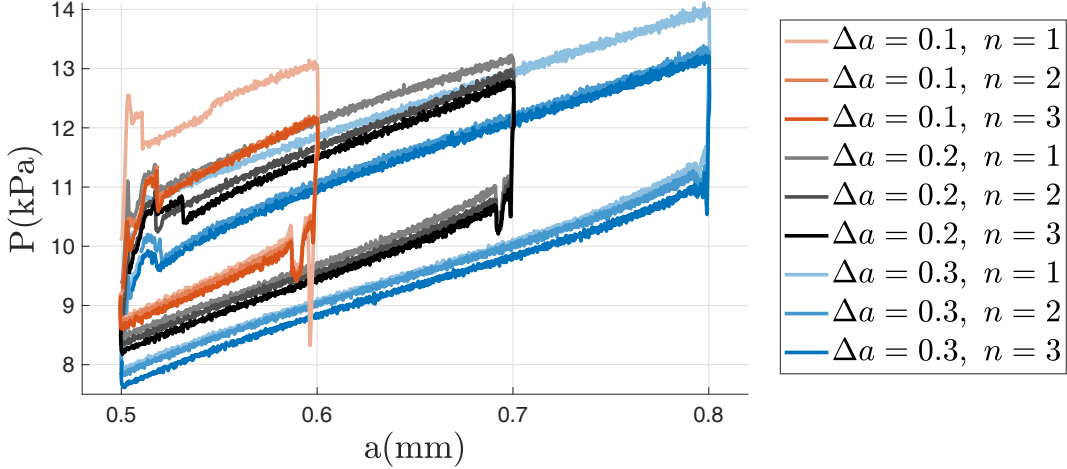


Figure 5: Demonstration of the Mullins effect in cavity expansion setting for PDMS sample S50-00 (see Section 7). Within an activated stretch range, there is a large difference in the material response from the first cycle to the second but thereafter remains unchanged over subsequent cycles. Hysteresis is observed between loading and unloading. The sharp pressure drop when the loading rate is reversed at the maximum cavity size is an indicator of rate dependent material response.

### 3.7. Loading protocol

A crucial difference between the experimental method in this paper, and existing cavity based experimental approaches, is the use of constant cavity expansion rates ( $\dot{a} = \text{const}$ ) instead of the typical constant fluid volume flow rate  $Q$ . The use of constant volume flow rate  $Q$  ( $= 4\pi a^2 \dot{a}$ ) in the expansion of a small initial cavity results in significant variation in the cavity stretch rate  $\dot{\lambda}_a$  ( $= \dot{a}/A$ ) during expansion, and in especially high cavity stretch rates at small  $a$ . This is shown in Figure 6 for the flow rates employed in Raayai-Ardakani et al. (2019a). We later demonstrate in Section 6.3 that, for the materials used in this work, such volume flow rates (which are typically used in ‘quasistatic’ cavity based experiments) activate high stretch rate response. Hence, the inference that the experiments were conducted quasi-statically is incorrect. Nonetheless, it is confirmed that the pressure profiles show little rate dependence, since the material response saturates for the high stretch rates activated.

After cavity initiation and removal of Mullins effect, as described earlier, we begin our main loading protocol. We cycle at constant cavity expansion rates between effective cavity sizes  $a_1 = 0.6$  mm and  $a_2 = 0.8$  mm. These cavity sizes comfortably fall within the fracture free range we identified for the material systems considered here and can be modified for other materials. The retraction from  $a_2$  to  $a_1$  is always performed at the minimum rate  $\dot{a} = -0.01$  mm/s to prevent detachment of fluid and plunger whereas the expansion rate is doubled between every expansion from a value of  $\dot{a} = 0.02$  mm/s to  $\dot{a} = 0.32$  mm/s. At the end of each expansion and retraction, the cavity is given time of  $t_{\text{wait}} = 400$  s to relax. This is clarified in Table 2 where the entire protocol discussed in this section has been summarized.

Representative figures of typical pressure profiles that result from this experimental protocol are shown in Figure 7 for one loading cycle. The time elapsed in a given cycle is identified by  $t_{\text{rel}}$  which is zeroed at the start of every cycle. The expansion starts at  $t_{\text{rel}} = t_1$  and ends at  $t_{\text{rel}} = t_2$  after which the material is allowed to relax at a constant stretch, up to  $t_{\text{rel}} = t_3$ .

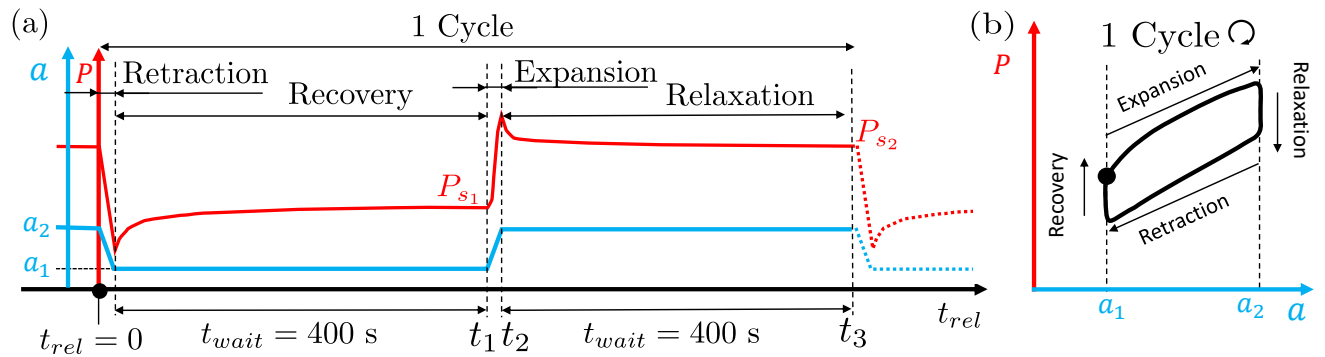
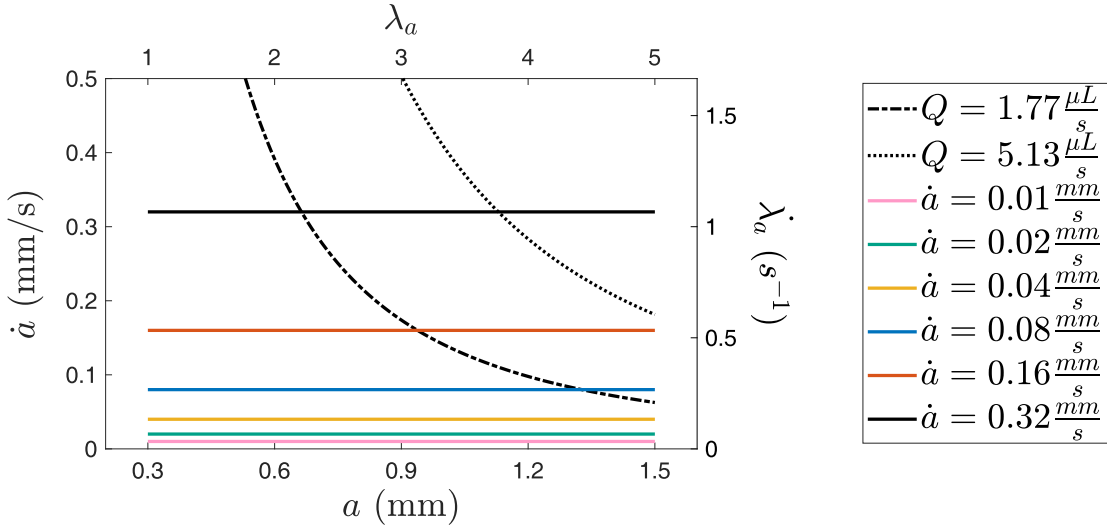


Table 2: Full experimental protocol for probing viscoelastic rate dependent material response using VCCE.

Assembly:	Fill and install the syringe-sensor assembly while avoiding air entrapments.
Calibration for dynamic pressure correction:	Inject needle in container of working fluid and perform full retraction, expansion cycles for all testing cycles. Record $\Delta p_{dyn}(a, \dot{a})$ for pressure correction.
Balance:	Remove fluid container, eject fluid droplet to ensure needle is completely filled. Wait 10 s to determine ambient pressure $p_{atm}$ . Balance Input displacement ( $z = 0$ ).
Insertion and initiation:	Insert needle in sample till surface ruptures, and immediately retract until $p \gtrsim 0$ . Expand initial cavity to $a = 0.5$ mm, give time to relax fully ( $t_{wait} \approx 1$ hour).

Mullins effect removal:	Increase volume to $a_1 = 0.6$ mm, let relax fully ( $t_{wait} \approx 1$ hour). Increase volume to $a_2 = 0.8$ mm, let relax fully ( $t_{wait} \approx 1$ hour).
Cycle 0 (confirmation of Mullins effect removal):	Retract at $\dot{a} = -0.01$ mm/s ( $a_2 \rightarrow a_1$ ), $t_{wait} = 400$ s. Expand at $\dot{a} = 0.01$ mm/s ( $a_1 \rightarrow a_2$ ), $t_{wait} = 400$ s. Repeat 3 times.
Cycles 1 - 5:	For $i = 1$ to 5, $\dot{a}_i = 0.02$ mm/s, do { Retract at $\dot{a} = -0.01$ mm/s ( $a_2 \rightarrow a_1$ ), $t_{wait} = 400$ s. Expand at $\dot{a}_i$ ( $a_1 \rightarrow a_2$ ), $t_{wait} = 400$ s. $\dot{a}_{i+1} = 2\dot{a}_i$ }

#### 4. Representative experimental results

Having defined the full experimental protocol, we first show representative results for soft PDMS (Polydimethylsiloxane) rubber sample (Sylgard 184, Dow Corning) with base:cross-linking agent ratio of 50:1 (more details on the sample and its preparation follow in Section 7). The surface tension correction is done using  $\gamma = 40$  mN/m (Ismail et al., 2009; Fox et al., 1947). The corrected gauge pressure is plotted in Figure 8, both as a function of the effective cavity size  $a$  and as a function of time. The first thing to note is that pressure profiles for the three cycles of loadings in Figure 8(a) for the expansion rate  $\dot{a} = 0.01$  mm/s (Cycle 0) coincide. This both confirms the removal of Mullins effect and demonstrates the remarkable precision and control that follows from the experimental protocol detailed in the previous section. *Furthermore, the change in expansion pressure profile with increasing expansion rate is a clear signature of rate dependent material response.* The peak pressure for every cycle,  $P_{max}$ , is attained whenever the maximum cavity size  $a = a_2$  is first reached ( $t_{rel} = t_2$ ) and is higher for higher expansion rates. Since the retraction is always performed at  $\dot{a} = -0.01$  mm/s, the retraction pressure profiles nearly coincide. Stress relaxation happens while the cavity size is held constant at  $a = a_2$ , which causes the pressure to drop with time to an equilibrium value  $P_{s2}$  (also shown in Figure 7). Conversely, stress recovery occurs while the cavity size is held constant at  $a = a_1$ , which causes the pressure to increase to an equilibrium value  $P_{s1}$ . The relaxation and recovery consistently result in approximately similar equilibrated pressure values over all the cycles, indicating that the equilibrium elastic part of the material response is well captured. There is a however slight decay in the equilibrated pressure values between cycles (<3% over all cycles). The monotonous nature of the decay seems to indicate there might be fatigue due to damage accumulation over multiple cycles. However, it could also indicate ongoing relaxation at material timescales much larger than the experimental timescale.

We quantitatively qualify the change in material resistance with loading rates by defining the dynamic amplification ratio  $R_P$ ,

$$R_P = (P_{max} - P_{s1}) / (P_{s2} - P_{s1}) \quad (5)$$

For the experimental data shown in Figure 8, we obtain approximate  $R_P$  values of 1.4, 1.5, 1.6, 1.8, 2.0 and 2.4, corresponding to Cycle 0 to Cycle 5. Since  $R_P = 1$  for quasistatic loading, even the slowest expansion rate considered here shows dynamic amplification of 40% in the pressure response. Thus, any consideration of the experiment to have been conducted quasistatically would be untenable. Modelling of the rate dependent material response then becomes essential and is the subject of our next section.

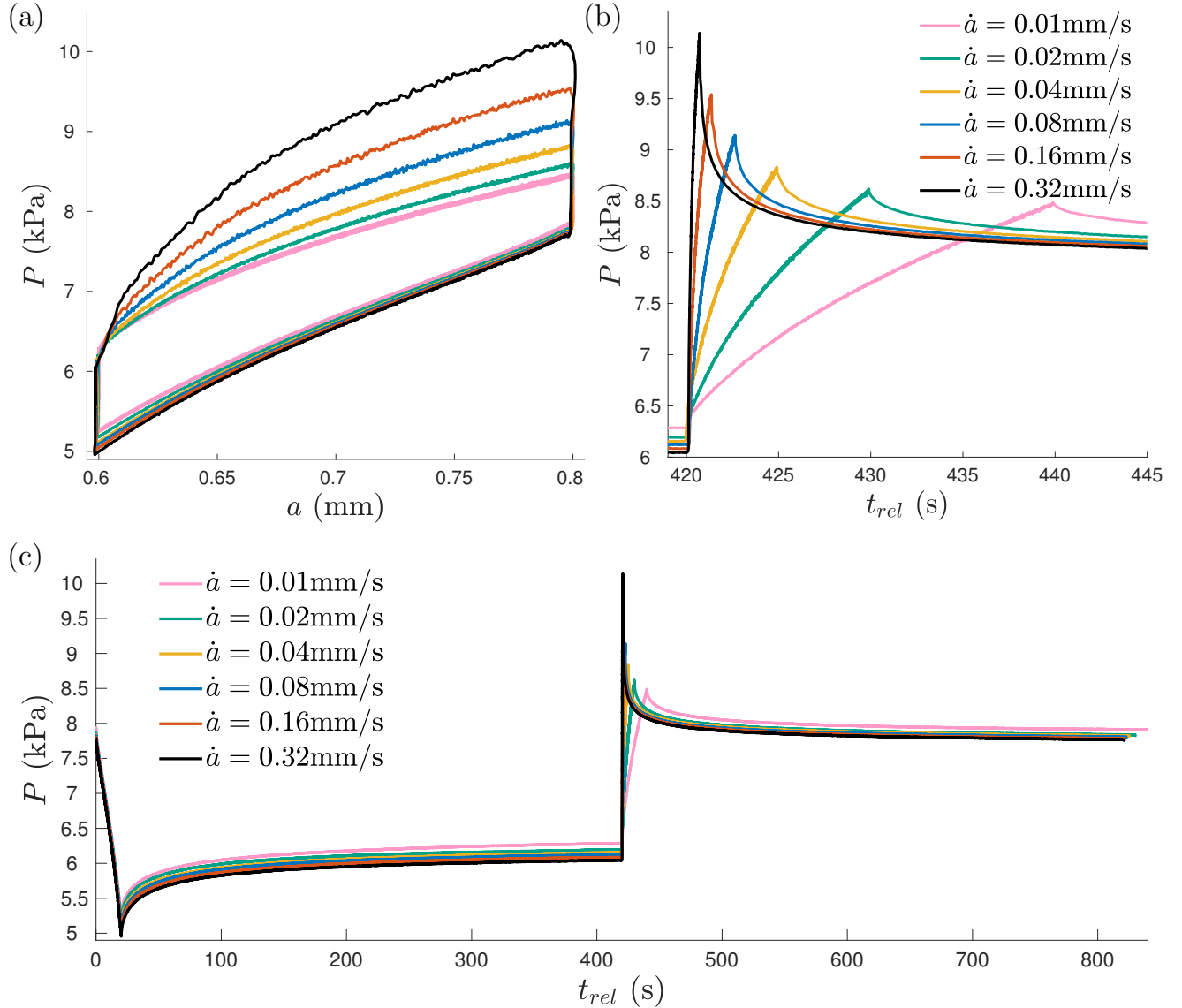


Figure 8: Experimental gauge pressure data for soft PDMS rubber sample with base:cross-linking agent ratio of 50:1 (sample S50-00 of Section 7). (a) Pressure data as a function of effective cavity size  $a$ . (b) Pressure data as a function of time, for the expansion response. (c) Complete pressure-time profiles.

## 5. Governing equations and generalized nonlinear viscoelastic model

### 5.1. Constitutive response

To model the viscoelastic response of a general nonlinear isotropic, and incompressible material, we follow the constitutive modelling approach in Kumar and Lopez-Pamies (2016); Kumar et al. (2017); Ghosh and Lopez-Pamies (2020) with some modifications. Motivated by our experimental observations, we consider a generalized Maxwell rheological model with an equilibrium branch and  $N$  non-equilibrium branches as shown in Figure 9. To describe the response of each non-equilibrium branch, denoted by  $n = 1, 2, \dots, N$ , the deformation gradient  $\mathbf{F}$  is multiplicatively

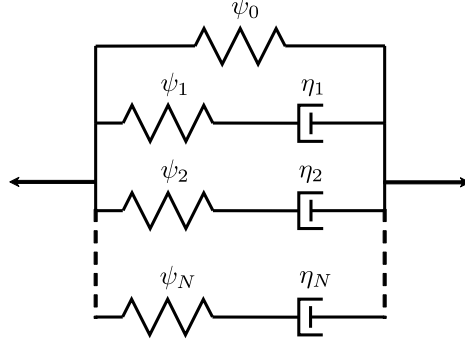


Figure 9: Generalized Maxwell rheological model considered in this paper with an equilibrium branch and  $N$  non-equilibrium branches. The equilibrium branch is described by a hyperelastic spring with free energy density  $\psi_0$  and the  $n^{\text{th}}$  non-equilibrium branch is described by a hyperelastic spring with free energy density  $\psi_n$  and a viscous dashpot with viscosity material parameter  $\eta_n$ .

decomposed as<sup>2</sup>

$$\mathbf{F} = \mathbf{F}_n^e \mathbf{F}_n^v \quad \text{for } n = 1, 2, \dots, N \quad (6)$$

where  $\mathbf{F}_n^v$  is the viscous distortion and  $\mathbf{F}_n^e$  is the non-equilibrium elastic distortion, in the  $n^{\text{th}}$  non-equilibrium branch. The viscous distortion  $\mathbf{F}_n^v$  is known at  $t = 0$  and evolves over time by a prescribed kinetic law. All the spring elements in the generalized Maxwell rheological model (Figure 9) are assumed to be incompressible and thus  $\det(\mathbf{F}) = \det(\mathbf{F}_n^e) = 1$  for  $n = 1, 2, \dots, N$ . The free energy density of the system is assumed to be of the form

$$\psi = \hat{\psi}_0(\mathbf{F}) + \sum_{n=1}^N \hat{\psi}_n(\mathbf{F}_n^e) = \hat{\psi}_0(\mathbf{F}) + \sum_{n=1}^N \hat{\psi}_n(\mathbf{F} \mathbf{F}_n^v \mathbf{F}^T) \quad (7)$$

where  $\psi_0$  and  $\psi_n$  are the free energy densities of the equilibrium and non-equilibrium branches respectively, and according to (6),  $\mathbf{F}_n^e = \mathbf{F} \mathbf{F}_n^v \mathbf{F}^T$ . The Cauchy stress tensor  $\boldsymbol{\sigma}$  is then given as

$$\boldsymbol{\sigma} = \frac{\partial \psi}{\partial \mathbf{F}} \mathbf{F}^T - p \mathbf{I} \quad (8)$$

where  $p$  is an arbitrary hydrostatic pressure associated with the incompressibility constraint. We prescribe the time evolution of the viscous distortion through a kinetic law for  $\mathbf{C}_n^v = \mathbf{F}_n^{vT} \mathbf{F}_n^v$ , that satisfies the second law of thermodynamics, isotropic symmetry and incompressibility requirements, and material frame indifference (see Appendix A.1),

$$\dot{\mathbf{C}}_n^v = \frac{2}{\eta_n I_{1n}^v} \left( \mathbf{F}_n^{vT} \mathbf{M}_n \mathbf{F}_n^v - \frac{1}{3} \text{tr}(\mathbf{M}_n) \mathbf{C}_n^v \right) \quad , \quad \mathbf{M}_n = \mathbf{F}_n^{eT} \frac{\partial \hat{\psi}_n}{\partial \mathbf{F}_n^e} \quad (9)$$

where  $I_{1n}^v = \text{tr}(\mathbf{C}_n^v)$ , and  $\eta_n$  is a positive viscosity material parameter associated with the  $n^{\text{th}}$  non-equilibrium branch.

---

<sup>2</sup>Repeated indices do not imply summation throughout this paper.

### 5.2. Spherically symmetric deformation

The geometry of a finite body with a cavity undergoing spherically symmetric expansion is illustrated in Figure 1(b). The body is loaded by internal and external pressures  $p_a$  and  $p_b$  respectively, and the gauge pressure  $P$  is defined as  $P = p_a - p_b$ . The radial coordinate in the initial and deformed configurations is defined by  $R$  and  $r$ , respectively. The corresponding inner and outer radii of the body in the undeformed and deformed configurations are  $A$ ,  $B$  and  $a$ ,  $b$ , respectively. Limiting our attention to incompressible materials, the deformation gradient can be written in spherical basis as

$$\mathbf{F} = \begin{bmatrix} \lambda_r & 0 & 0 \\ 0 & \lambda_\theta & 0 \\ 0 & 0 & \lambda_\phi \end{bmatrix} = \begin{bmatrix} R^2/r^2 & 0 & 0 \\ 0 & r/R & 0 \\ 0 & 0 & r/R \end{bmatrix} \quad (10)$$

where  $\lambda_i$  ( $i = r, \theta, \phi$ ) are the principal stretches associated with  $\mathbf{F}$  and  $\lambda = \lambda_\theta = \lambda_\phi = r/R$  is the circumferential stretch. For the spherically symmetric deformation, the tensorial multiplicative decomposition (6) implies the following scalar decompositions for the principal stretches

$$\lambda_i = \lambda_{in}^e \lambda_{in}^v \quad \text{for } n = 1, 2, \dots, N \text{ and } i = r, \theta, \phi \quad (11)$$

where  $\lambda_{in}^e$  and  $\lambda_{in}^v$  ( $i = r, \theta, \phi$ ) are the principal stretches associated with  $\mathbf{F}_n^e$  and  $\mathbf{F}_n^v$ , respectively. Incompressibility conditions ( $\det(\mathbf{F}) = \det(\mathbf{F}\mathbf{F}_n^{v-1}) = 1$ ) and symmetry imply

$$(\lambda_{rn}^e)^{-1/2} = \lambda_{\theta n}^e = \lambda_{\phi n}^e \quad , \quad (\lambda_{rn}^v)^{-1/2} = \lambda_{\theta n}^v = \lambda_{\phi n}^v (= \lambda_n^v) \quad (12)$$

Additionally, for any spherical sub-region incompressibility implies

$$r^3 - a^3 = R^3 - A^3 \quad (13)$$

which for the entire body reads  $b^3 - a^3 = B^3 - A^3$ . The circumferential stretch can then be written in terms of the circumferential stretch at the cavity wall,  $\lambda_a$ , as

$$\lambda(R, t) = \frac{r(R, t)}{R} = \left( 1 + (\lambda_a^3(t) - 1) \left( \frac{A}{R} \right)^3 \right)^{1/3} ; \quad \lambda_a(t) = \frac{a(t)}{A} \quad (14)$$

The circumferential stretch at the outer radius of the body,  $\lambda_b$ , is thus given as

$$\lambda_b(t) = \lambda(B, t) = \frac{b(t)}{B} = \left( 1 + (\lambda_a^3(t) - 1) \left( \frac{A}{B} \right)^3 \right)^{1/3} \quad (15)$$

For modelling the experiments in this paper,  $B/A$  is taken to be 1000. We remark that the modelling results for an infinite solid ( $B/A \rightarrow \infty$ ) would be indistinguishable from the results for the  $B/A$  value chosen here, as shown in Raayai-Ardakani et al. (2019b).

The radial velocity and acceleration are derived from (13) as

$$\dot{r} = \frac{a^2 \dot{a}}{r^2} \quad ; \quad \ddot{r} = \frac{2a\dot{a}^2 + a^2\ddot{a} - 2r\dot{r}^2}{r^2} \quad (16)$$

Thus, the motion of the entire body is described by the motion of the inner cavity wall due to incompressibility. In what follows, we relate the motion of the cavity wall to the pressure loading  $P(t)$  by using the radial equation of motion and employing the constitutive model developed in the previous subsection.

### 5.3. Radial equation of motion

For the spherically symmetric deformation field, the only non-trivial equation of motion is along the radial direction

$$\frac{\partial \sigma_r}{\partial r} - \frac{2s}{r} = \rho \ddot{r} \quad (17)$$

where  $s = \sigma_\theta - \sigma_r$  is the difference between  $\sigma_\theta = \sigma_\phi$  and  $\sigma_r$ , namely the circumferential and radial principal Cauchy stress components, respectively, and  $\rho$  is the constant mass density. Substituting  $\ddot{r}$  from (16) in (17) and integrating over the whole body from  $r = a(t) = a\lambda_a$  to  $r = b(t)$  yields

$$P(t) = S(t) + P_{in}(t) \quad (18a)$$

$$P_{in}(t) = \rho A^2 \left[ \left( 2\dot{\lambda}_a^2 + \lambda_a \ddot{\lambda}_a \right) \left( 1 - \frac{\lambda_a A}{\lambda_b B} \right) - \frac{\dot{\lambda}_a^2}{2} \left( 1 - \frac{\lambda_a^4 A^4}{\lambda_b^4 B^4} \right) \right], \quad S(t) = \int_a^b \frac{2s}{r} dr \quad (18b)$$

where we have used the definitions for boundary stretches in (14)-(15) and employed the boundary conditions  $\sigma_r(r = a, t) = -p_a(t)$  and  $\sigma_r(r = b, t) = -p_b(t)$ . Note that the gauge pressure at the cavity wall  $P(t)$  differs from the gauge pressure inside the fluid in the cavity,  $P_f(t)$ , due to surface tension effect ( $P(t) = P_f(t) - 2\gamma/a(t)$ ) but this has already been accounted for in the experimental pressure curves, as seen in eq. (4). The term  $S(t)$  represents the pressure due to the elastic material resistance whereas  $P_{in}(t)$  is the pressure that results from inertial effects. The inertial term, for the slow expansion rates in our experiments, is insignificant<sup>3</sup> compared to the pressure generated due to elastic material resistance, but is nevertheless accounted for. Earlier derivation of the above relation can be found in Cohen and Molinari (2015). In the following subsection, we employ the constitutive model developed in Section 5.1 to evaluate the term  $S(t)$ .

---

<sup>3</sup>For our experimental protocol,  $\ddot{a}$  is theoretically unbounded at the end of expansion and retraction cycles but in reality the volume control by the testing machine causes smoothing of the time profile of  $a$  and thus results in finite  $\ddot{a}$ . The inertial pressures caused by these cavity wall accelerations are still insignificant compared to pressure arising from elastic material resistance.

#### 5.4. Constitutive model applied to equation of motion

For spherically symmetric deformation, the free energy density in (7) can be rewritten in terms of principal stretches as

$$\psi = \hat{\psi}_0(\mathbf{F}) + \sum_{n=1}^N \hat{\psi}_n(\mathbf{F}_n^e) = \bar{\psi}_0(\lambda_r, \lambda_\theta, \lambda_\phi) + \sum_{n=1}^N \bar{\psi}_n(\lambda_{rn}^e, \lambda_{\theta n}^e, \lambda_{\phi n}^e) \quad (19)$$

which, upon substitution of eqs. (11) and (12), can be rewritten in terms of  $\lambda$  and  $\lambda_n^v$ , as

$$\begin{aligned} \psi &= \bar{\psi}_0(\lambda^{-2}, \lambda, \lambda) + \sum_{n=1}^N \bar{\psi}_n \left( \left( \frac{\lambda_n^v}{\lambda} \right)^2, \frac{\lambda}{\lambda_n^v}, \frac{\lambda}{\lambda_n^v} \right) \\ &= \tilde{\psi}_0(\lambda) + \sum_{n=1}^N \tilde{\psi}_n(\lambda/\lambda_n^v) \end{aligned} \quad (20)$$

This free energy density results in the following expression for  $s = \sigma_\theta - \sigma_r$  (see Appendix A.2),

$$s = \frac{\lambda}{2} \tilde{\psi}'_0(\lambda) + \sum_{n=1}^N \frac{\lambda}{2\lambda_n^v} \tilde{\psi}'_n(\lambda/\lambda_n^v) \quad (21)$$

Using (13) to employ the transformation  $dr/r = d\lambda/(\lambda(1 - \lambda^3))$ , we rewrite eq. (18) using (21) as

$$P(t) = \int_{\lambda_a}^{\lambda_b} \frac{\tilde{\psi}'_0(\lambda)}{1 - \lambda^3} d\lambda + \sum_{n=1}^N \int_{\lambda_a}^{\lambda_b} \frac{\tilde{\psi}'_n(\lambda/\lambda_n^v)}{\lambda_n^v(1 - \lambda^3)} d\lambda + P_{in}(t) \quad (22)$$

where  $\lambda_a$  and  $\lambda_b$  are defined in eqs. (14) and (15). The evolution law (9) defines the viscous stretch  $\lambda_n^v$  implicitly through the differential equation (see Appendix A.2)

$$\dot{\lambda}_n^v = \frac{\lambda}{6\eta_n I_{1n}^v} \tilde{\psi}'_n(\lambda/\lambda_n^v) \quad (23)$$

along with an initial condition for  $\lambda_n^v(R, t=0)$ .

Finally, for a prescribed deformation of the cavity wall,  $\lambda_a(t) = a(t)/A$ , using the relations in eqs. (14) and (15), eq. (23) can be integrated over time to evaluate the pressure variation in eq. (22) where  $P_{in}(t)$  is defined in (18). The first term in the right hand side of eq. (22) corresponds to the pressure due to the elastic part of the response that is in thermodynamic equilibrium. The second term is the pressure that arises from the elastic part of the response that is not in thermodynamic equilibrium, namely, the elastic part that decays in time through viscous dissipation. It remains to prescribe specific free energy functions, which are chosen next to best represent the experimental results.

### 5.5. Choice of free energy functions

Following previous experimental cavity expansion studies, we employ the incompressible neo-Hookean free energy functions, which we find sufficient to capture the material response,

$$\hat{\psi}_0(\mathbf{F}) = \frac{E}{6} (I_1 - 3) \quad , \quad \hat{\psi}_n(\mathbf{F}\mathbf{F}_n^{v-1}) = \frac{\alpha_n E}{6} (I_{1n}^e - 3) \quad \text{for } n = 1, 2, \dots, N \quad (24)$$

where  $I_1 = \text{tr}(\mathbf{C})$  and  $I_{1n}^e = \text{tr}(\mathbf{C}\mathbf{C}_n^{v-1})$  with  $\mathbf{C} = \mathbf{F}^T\mathbf{F}$  and  $\mathbf{C}_n^v = \mathbf{F}_n^{vT}\mathbf{F}_n^v$ . The non-negative material parameter  $\alpha_n$  is the ratio of the modulus of the  $n^{\text{th}}$  non-equilibrium branch to the modulus  $E$  of the equilibrium branch. In general we can choose different free energy functions for the different branches of the rheological model (Figure 9), where the chosen free energy functions can have more material parameters than the above neo-Hookean model, which requires only one parameter (the modulus) per branch. The choice of free energy functions can have non-trivial consequences for nonlinear phenomena observed in other deformation modes, see for example Chockalingam and Cohen (2020).

For the free energy functions in eq. (24), the Cauchy stress is readily derived using (8) as

$$\boldsymbol{\sigma} = \frac{E}{3} \mathbf{F} \mathbf{F}^T + \sum_{n=1}^N \frac{\alpha_n E}{3} \mathbf{F} \mathbf{C}_n^{v-1} \mathbf{F}^T - p \mathbf{I} \quad (25)$$

whereas the evolution law (9) specializes to

$$\dot{\mathbf{C}}_n^v = \frac{8}{\tau_n I_{1n}^v} \left( \mathbf{C} - \frac{1}{3} (\mathbf{C} \cdot \mathbf{C}_n^{v-1}) \mathbf{C}_n^v \right) \quad , \quad \tau_n = \frac{12\eta_n}{\alpha_n E} > 0 \quad (26)$$

The viscous material parameter  $\tau_n$  quantifies the timescale over which stress in the  $n^{\text{th}}$  non-equilibrium branch decays in a stress relaxation experiment. Further, eq. (22) simplifies to

$$P(t) = \frac{E}{6} (4\lambda_b^{-1} + \lambda_b^{-4} - 4\lambda_a^{-1} - \lambda_a^{-4}) + \sum_{n=1}^N \int_{\lambda_a}^{\lambda_b} \frac{\tilde{\psi}'_n(\lambda/\lambda_n^v)}{\lambda_n^v(1-\lambda^3)} d\lambda + P_{in}(t) \quad (27)$$

where

$$\tilde{\psi}_n(\lambda/\lambda_n^v) = \frac{\alpha_n E}{6} \left( 2 \left( \frac{\lambda}{\lambda_n^v} \right)^2 + \left( \frac{\lambda}{\lambda_n^v} \right)^{-4} - 3 \right) \quad (28)$$

and the evolution law (26) defines the viscous stretch  $\lambda_n^v$  implicitly through the differential equation

$$\dot{\lambda}_n^v = \frac{4}{3\tau_n} \frac{1}{(2\lambda_n^{v2} + \lambda_n^{v-4})} \left( \frac{\lambda^6 - \lambda_n^{v6}}{\lambda_n^v \lambda^4} \right) \quad (29)$$

and an initial condition for  $\lambda_n^v(R, t=0)$ , as described next.

### 5.6. Initial conditions

Integration of (29) for the viscous stretch  $\lambda_n^v(R, t)$  requires an initial condition. For our experiments, we perform separate time integrations for the expansion-relaxation and retraction-recovery part of every loading cycle. For the initial condition at the start of every expansion

or retraction, we assume that the material is fully relaxed/recovered, i.e. that the contributions to the gauge pressure from the non-equilibrium branches have died out in eq. (27). This yields the initial condition  $\lambda_n^v(R, t_{start}) = \lambda(R, t_{start})$  where  $t_{start}$  is the time when the corresponding expansion or retraction begins and  $\lambda(R, t_{start})$  is determined from (14) given  $\lambda_a(t_{start})$ .

## 6. Fitting procedure

Having prescribed the constitutive model, the associated material parameters remain to be estimated from the experimentally measured pressure response. By isolating the equilibrated part of the measured pressure response, the equilibrium branch modulus  $E$  and the effective stress free size of the initial defect,  $A$ , are first estimated independent of the dynamic pressure response. The non-equilibrium branch parameters are subsequently estimated from a best fit to the dynamic part of the measured pressure response.

### 6.1. Quasistatic parameters

The equilibrated pressures at the start and end of the expansion-relaxation part of any cycle ( $P_{s1}, P_{s2}$ ) are related to the equilibrium branch response, after the contributions from the non-equilibrium branches have died away, as seen from<sup>4</sup> (27) . Thus the equilibrated pressures at  $(a_1, t_1)$  and  $(a_2, t_2)$  are used to estimate the values of  $E$  and  $A$ ,

$$P_{s1} = \frac{E}{6} (4\lambda_{b1}^{-1} + \lambda_{b1}^{-4} - 4\lambda_{a1}^{-1} - \lambda_{a1}^{-4}) \quad , \quad P_{s2} = \frac{E}{6} (4\lambda_{b2}^{-1} + \lambda_{b2}^{-4} - 4\lambda_{a2}^{-1} - \lambda_{a2}^{-4}) \quad (30)$$

where  $\lambda_{a_i} = a_i/A$  ( $i = 1, 2$ ) and  $\lambda_{b_i}$  is related to  $\lambda_{a_i}$  using (15). The estimated values of  $E$  and  $A$  from the equilibrated pressures of each loading cycle, for the representative sample S50-00, can be seen to be approximately constant in Table 3 (second and third columns). This is a consequence of the fact that the experimental equilibrated pressures do not vary much across loading cycles. The slight but steady increase in the value of  $A$  across cycles is attributed to likely fatigue/damage, as discussed in Section 4. We note here that while our estimated equilibrium elastic modulus is about 15 kPa, the regular VCCE technique reports a significantly higher modulus of about 75 kPa and the Cavitation Rheology technique reports a modulus of about 25 kPa, for the same material composition (Raayai-Ardakani et al., 2019a). One source of discrepancy is the fact that we have eliminated the Mullins effect which results in some softening. However, a greater discrepancy arises from the choice of loading protocol as elaborated in Section 6.3.

### 6.2. Dynamic parameters

The remaining non-equilibrium material parameters are estimated using a nonlinear least squares fitting method that employs a material subroutine to integrate eqs. (27) and (29). The integration and fitting procedure are described in more detail in Appendix A. While our experimental cavity expansion protocol (Figure 8) includes multiple cycles of expansion and relaxation followed by retraction and recovery, parameter fitting can either be optimized for the entire time of the experiment or for specific sub-intervals. In this work, we conduct the fitting on the

---

<sup>4</sup>Inertial pressure  $P_{in}(t)$  also vanishes at the equilibrium states since cavity stretch  $\lambda_a$  is held constant.

expansion-relaxation part of the material response<sup>5</sup>. Nonetheless, as a validation, the fitted parameters will be seen to also capture the retraction-recovery profiles well. For our experimental results, we find that two non-equilibrium branches ( $N = 2$ ) and thus four non-equilibrium parameters ( $\alpha_1, \alpha_2, \tau_1, \tau_2$ ) are sufficient to capture the experimentally measured material response. While a different choice of the kinetic evolution law, instead of eq. (26), could possibly capture the experimental response well using a single non-equilibrium branch, there is no straightforward way to determine such an optimal kinetic law. Among the different kinetic laws we surveyed, the chosen evolution law in eq. (26) performs the best in capturing the experimental results.

Representative fitted parameters obtained by individually fitting to the expansion-relaxation part of each loading cycle of the experimental curves for sample S50-00, are shown in Table 3. It is seen that the estimated non-equilibrium branch parameters exhibit a moderate dependence on the expansion rate. This dependence could potentially be reduced by optimizing the kinetic evolution law, by either varying the free energy functions of the non-equilibrium branches ( $\psi_n$ ), or by choosing a different form of the evolution law (23). Nonetheless, any fitted model can only be optimized to perform within the range of expansion rates probed in the experiment. In this work, to obtain a best fit for the entire range of expansion rates across all loading cycles using a single set of parameters, we examine the error associated with the fitted dynamic parameters of the individual cycles, when used to predict the pressure for all loading cycles while using the values of  $E$  and  $A$  fitted for the corresponding cycles<sup>6</sup>.

Table 3: Fitting parameters for representative sample S50-00 (see Sections 4 and 7).

Fitting Cycle	$\dot{a}$ (mm/s)	$A$ (mm)	$E$ (kPa)	$\alpha_1$	$\tau_1$ (s)	$\alpha_2$	$\tau_2$ (s)
1	0.02	0.353	14.71	0.597	2.76	0.097	154.63
2	0.04	0.356	14.77	0.789	1.54	0.109	129.07
3	0.08	0.358	14.77	0.927	1.00	0.116	123.18
4	0.16	0.360	14.79	1.246	0.56	0.128	110.56
5	0.32	0.363	14.83	1.599	0.32	0.140	97.16

To evaluate the fit of a given set of parameters on a single loading cycle, we define the following errors

$$\epsilon = \sqrt{\frac{\int_{t_1}^{t_3} (P - P_e)^2 dt_{rel}}{\int_{t_1}^{t_3} P_e^2 dt_{rel}}}, \quad \epsilon_{exp} = \sqrt{\frac{\int_{t_1}^{t_2} (P - P_e)^2 dt_{rel}}{\int_{t_1}^{t_2} P_e^2 dt_{rel}}}, \quad \epsilon_{max} = \max_{t_{rel} \in [t_1 t_3]} \left( \left| \frac{P - P_e}{P_e} \right| \right) \quad (31)$$

where  $P$  is the gauge pressure predicted by the viscoelastic material model for the given set of parameters and  $P_e$  is the experimentally measured gauge pressure. The fitting error for the time of the entire expansion-relaxation is estimated by  $\epsilon$  whereas  $\epsilon_{exp}$  denotes the fitting error on the expansion part of the loading cycle alone. The integrals in (31) are evaluated numerically using

<sup>5</sup>There is no possibility of separation of syringe plunger and fluid during expansion-relaxation and as such the pressure data can be regarded to be more reliable than for retraction-recovery.

<sup>6</sup>This is because we assume that there is slight fatigue between cycles that is not accounted for in the material model and the variation in the fitted values for  $E$  and  $A$  across the loading cycles is small.

a trapezoidal rule since the pressure data is discrete. To evaluate the fit over all loading cycles for a given set of material parameters we define the following overall errors

$$\epsilon^{tot} = \text{mean}_{\text{all cycles}} \epsilon, \quad \epsilon_{exp}^{tot} = \text{mean}_{\text{all cycles}} \epsilon_{exp}, \quad \epsilon_{max}^{tot} = \max_{\text{all cycles}} \epsilon_{max} \quad (32)$$

The material parameters that give the lowest overall errors are reported as the optimal fitted

Table 4: Errors in the pressure predicted by the viscoelastic material model, for all loading cycles, using dynamic material parameters fitted on Cycle 3 (third row in Table 3), for representative sample S50-00.

Cycle	$\dot{a}$ (mm/s)	$\epsilon$ (%)	$\epsilon_{exp}$ (%)	$\epsilon_{max}$ (%)
1	0.02	0.32	1.22	1.76
2	0.04	0.33	1.01	2.12
3	0.08	0.36	0.47	2.67
4	0.16	0.38	1.43	4.02
5	0.32	0.43	2.78	6.75
$\epsilon^{tot}$ (%) = 0.36 $\epsilon_{exp}^{tot}$ (%) = 1.38 $\epsilon_{max}^{tot}$ (%) = 6.74				

parameters for the material<sup>7</sup>. For the representative sample S50-00, the dynamic parameters fitted on Cycle 3 yield the lowest overall errors for pressure prediction across all loading cycles. The prediction errors for individual cycles using these optimal parameters are reported in Table 4. It can be seen that a single set of parameters can accurately predict the pressure response over the entire expansion-relaxation process for all loading cycles (stretch rates spanning  $10^{-2}$  -  $1 s^{-1}$ ), with the maximum absolute relative error always less than 7%. The predicted material response using these parameters is visually compared with the experimental curves in Figure 10, where it is seen that the retraction-recovery part of the response is also well predicted.

### 6.3. A cautionary note on viscoelastic effects in constant volumetric rate expansion

We now use the fitted material parameters from the previous section to explain both the lack of rate dependence observed in the pressure response in the VCCE experiments of Raayai-Ardakani et al. (2019a), as well as the significantly higher modulus values reported therein. Recall that the main difference between the experimental protocol in Raayai-Ardakani et al. (2019a) compared with the present work, is the expansion process. Here we consider constant rate radial expansion (i.e.  $\dot{a} = \text{const}$ ) in contrast to constant volume expansion rate (i.e.  $Q = 4\pi a^2 \dot{a} = \text{const}$ ), as discussed in Section 3.7.

Using the optimal fitted material parameters (third row of Table 3) for sample S50-00, we perform numerical integration to predict the pressure response for the case of constant volume expansion rate  $Q$ , starting at an undeformed cavity size  $A$  at  $t = 0$ . Accordingly, the cavity size as a function of time is given by

$$a(t) = \left( \frac{3Qt}{4\pi} + A^3 \right)^{1/3} \quad (33)$$

---

<sup>7</sup>For reporting optimal values for  $E$  and  $A$ , we use their fitted values from the cycle whose fitted dynamic parameters give the lowest overall errors.

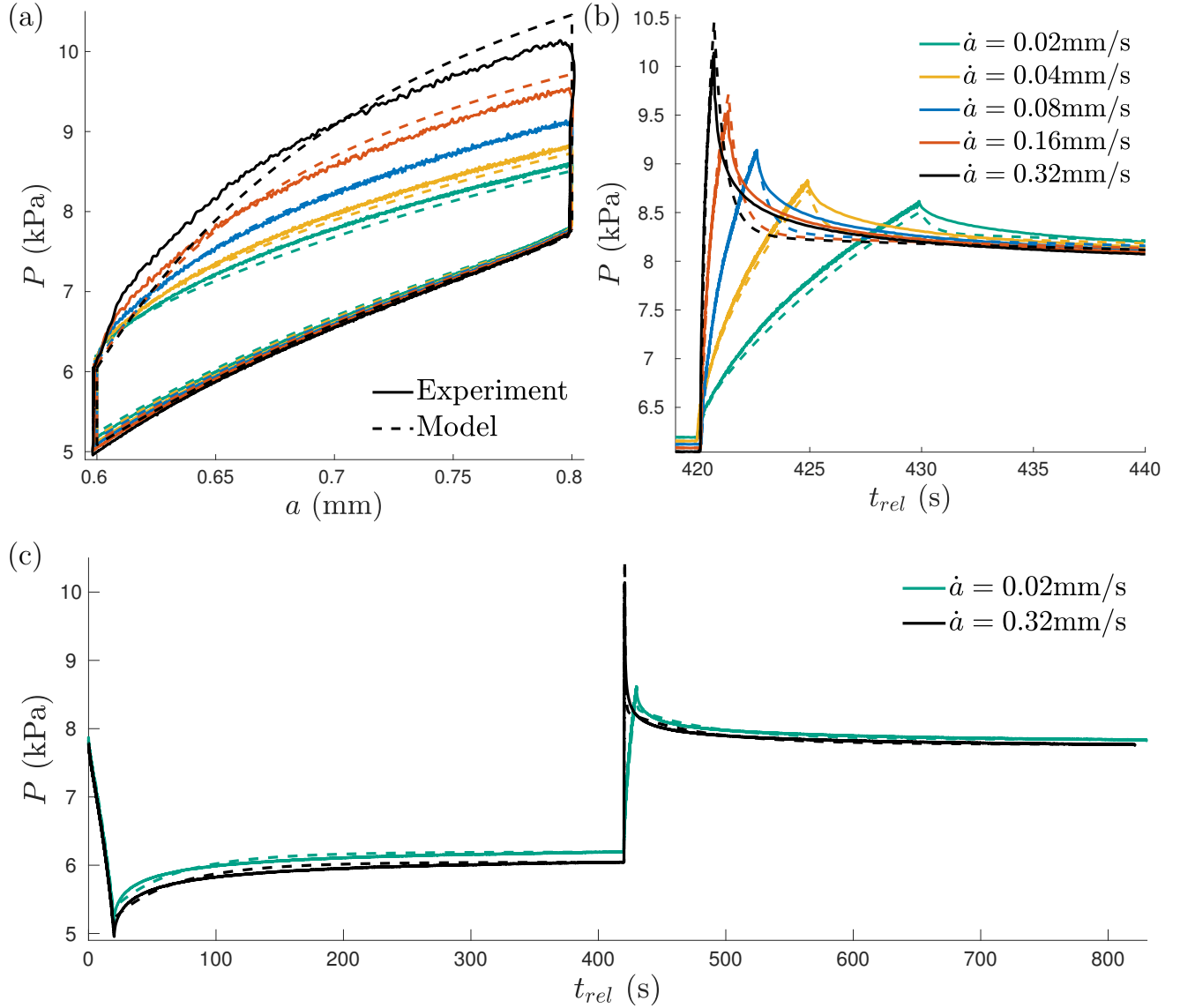


Figure 10: Comparison of the pressure response predicted by the viscoelastic material model with the experimental pressure data. The non-equilibrium material parameters fitted to loading Cycle 3 (Table 3) have been used to predict the pressure response for all loading cycles. The responses for only the extreme loading rates are shown in (c) to avoid clutter.

We consider  $A = 0.35 \text{ mm}$  and use the four volumetric rates reported in Raayai-Ardakani et al. (2019a), namely  $Q = 1.77, 2.95, 4.12, 5.13 \mu\text{L/s}$ , to integrate the material model for the pressure response. The resulting pressure versus cavity stretch curves are plotted in Figure 11(a). Almost no rate dependence is seen among the pressure curves for the four different seemingly small volumetric rates, at least until larger stretches are accessed. This lack of rate dependence is consistent with the experimental observations of Raayai-Ardakani et al. (2019a) and other needle based cavity expansion studies. For comparison, the integrated results for the case of constant cavity stretch rate loadings ( $a = \dot{a}t$ ) are shown in Figure 11(b), for the same material parameters with the expansion starting from the same undeformed cavity size  $A = 0.35 \text{ mm}$ . The rate dependent material response can be easily seen from these curves throughout the expansion.

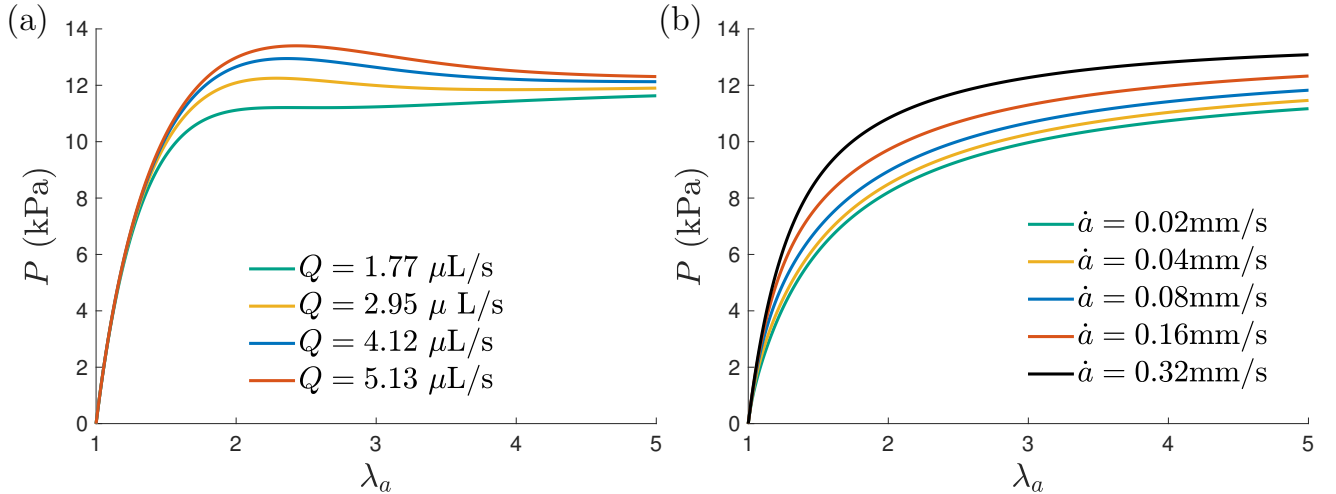


Figure 11: Pressure versus cavity stretch response predicted by the optimal fitted viscoelastic material parameters for sample S50-00, for different loading scenarios. (a) The volume expansion rate  $Q$  is constant. There is not much rate dependence observed during the expansion until high stretches are accessed and the pressure can drop for high stretch values. (b) The cavity stretch rate  $\dot{\lambda}_a = \dot{a}/A$  is constant. Rate dependence can be clearly seen and there is no pressure drop even at high stretches.

As explained earlier in Section 3.7, if the initial cavity size is sufficiently small in a spherical expansion setting, even small volumetric rates can result in high stretch rates initially. This explains the apparent saturation of the dynamic material response observed in Figure 11(a).

To further understand this response and its effect on the measurement of the elastic properties, we can write the instantaneous modulus,  $E_{inst}$ , for the rheological model in Figure 9 with  $N = 2$  and with the free energy functions chosen in eq. (24), as

$$E_{inst} = E(1 + \alpha_1 + \alpha_2) \quad (34)$$

This is the effective dynamic modulus of the material before onset of appreciable viscoelastic effects. Given the rate-insensitive response shown for moderate stretch levels in Figure 11(a), it is expected that a purely hyperelastic fit (only equilibrium branch free energy) would yield the instantaneous modulus, which according to the fitted values for  $\alpha_1$  and  $\alpha_2$  in Table 3 can over estimate the equilibrium modulus  $E$  by more than 250 %. This would in part explain the higher modulus values reported for the same PDMS composition in Raayai-Ardakani et al. (2019a) and consistently reported in other cavity expansion studies, as reviewed in more detail by Yang et al. (2019). Therein, several explanations of this effect are hypothesized, including strain stiffening effects that are not accounted for in the neo-Hookean model, and residual stresses induced by the embedded needle. However, the considerable influence of viscoelasticity has not been previously indicated. This emphasizes the need for stretch rate controlled VCCE experiments that can account for viscoelastic effects to accurately capture the material parameters.

An additional artifact of the constant volumetric rate expansion is the overshoot of the pressure, as observed by the appearance of peak values in Figure 11(a). Although the cavity continues to expand, the stretch rate decreases with increasing expansion ( $\dot{a} = Q/(4\pi a^2)$ ), thus the material response transitions from the stiffer, instantaneous, behavior characterised by the instantaneous modulus  $E_{inst}$ , to the softer behavior characterised by the equilibrium stiffness  $E$ . Note that

this transition is radially dependent, and the viscoelastic stiffening is most noticeable in the near vicinity of the cavity.

For the experiments in Raayai-Ardakani et al. (2019b), fracture, characterised by sharp sudden drop in pressure as opposed to the smooth and slight decrease in Figure 11(a), is observed at such high stretches. For the constant cavity stretch rate expansion the pressure does not drop even for high stretches, implying that a pressure drop would have to arise solely from fracture<sup>8</sup>, thus making it an even more attractive choice of loading protocol.

## 7. Characterising the viscoelastic response of tuneable PDMS samples

Having established the experimental method and the fitting of the experimental results to a generalized viscoelastic material model, we now apply our technique to study the viscoelastic response of soft PDMS rubber samples with tuneable content of non-reactive Silicone (PDMS) oil. This approach is inspired from the fracture study of such a system by Yang et al. (2019). Here we aim to examine the ability of our technique to capture changes in the constitutive response, which in this case are due to the oil content.

### 7.1. Sample preparation

The Sylgard 184 (Dow Corning) PDMS base is diluted with different weight percent of non-reactive PDMS oil ( $\mu$ MicroLubrol - 350cSt). The diluted PDMS mixture is then mixed with cross-linker to obtain different PDMS to cross-linker mass ratios (PDMS:CL), as defined in Table 5. Note that, in contrast to the fabrication procedure in Yang et al. (2019), where a base and cross-linker mix with a given mass ratio is subsequently diluted with oil, here we conserve the total mass fraction of the cross-linker to PDMS content including both the base and non-reactive oil. The final mixture of base, oil, and cross-linker, is homogenized in two cycles in a planetary centrifugal mixer. The mix is poured into plastic sample cups (dimensions -  $\varnothing$  2.5" x 1.75" height) and subsequently degassed in a desiccator for approximately 1 hour. The samples are cured in an oven at 100°C for 2 hours and then left to cool at room temperature. All tests are performed 2 - 3 weeks after cure.

### 7.2. Results

The full experimental protocol described in Table 2 was carried out for all the material samples listed in Table 5. The resulting pressure profiles are shown in Figure 12. It can clearly be seen that increasing Silicone oil content, for a given cross-linker mass fraction, leads to decreasing rate dependence of the material response. Plots of the dynamic amplification ratio, defined in eq. (5), are shown in Figure 13(a). The ratio increases with cavity expansion rates for all samples, indicating that the dynamic material stiffening (compared to the quasistatic response) is higher at higher stretch rates. The ratio also decreases with increasing Silicone oil content, for a given cross-linker mass fraction, at all expansion rates. This is consistent with the observation of decreasing rate dependence with increasing Silicone oil content, for a given cross-linker mass fraction. We also note that the equilibrated pressures show more variation across the loading cycles with increasing Silicone oil content, with the largest variation of about 1.5 kPa. This could be an indicator of possibly more pronounced fatigue effects with increasing oil content.

---

<sup>8</sup>The pressure can drop even for constant stretch rate loadings at very large stretches, however the material would fracture much earlier in reality.

Table 5: Sample compositions. The Sylgard 184 PDMS base is diluted with non-reactive Silicone (PDMS) oil. The diluted PDMS mixture is mixed with cross-linker to obtain different PDMS mix to cross-linker mass ratios (PDMS:CL).

Sample Reference	Composition		Effective Mass Ratio		
	PDMS:CL	Oil	Base	Oil	Cross-linker
S50-0	50:1	0%	50	0	1
S50-10	50:1	10%	45	5	1
S50-20	50:1	20%	40	10	1
S48-0	48:1	0%	48	0	1
S48-10	48:1	10%	43.2	4.8	1
S48-20	47.3:1	20%	37.8	9.5	1

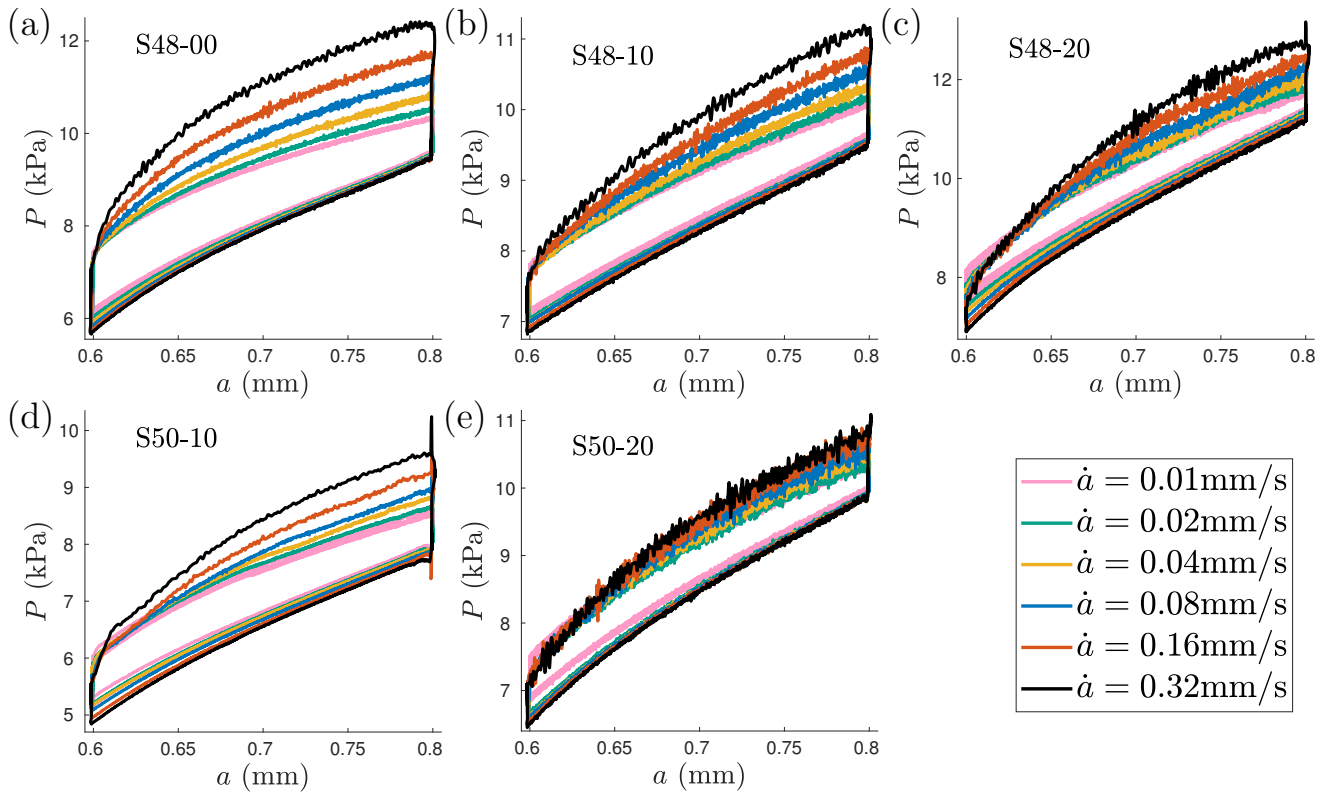


Figure 12: Experimental pressure profiles for the tuneable PDMS-Silicone oil system discussed in Section 7. Compositions for the different samples are listed in Table 5. The profile for sample S50-00 is shown in Figure 8. Increasing oil content can be seen to reduce the rate dependence of the material response.

The optimal fitted material parameters for all the samples along with the prediction errors are recorded in Table 6. For the chosen evolution law (29), two non-equilibrium branches were necessary to capture the experimentally observed material response, and the fitted parameters for  $\tau_1$  and  $\tau_2$  indicate the presence of two distinct timescales of relaxation. The parameters fitted to individual cycles, for all samples, are listed in Appendix B. The effective size of the stress free cavity,  $A$ , does not vary much across all samples tested here, implying that all the

Table 6: Optimal fitted material parameters for all samples listed in Table 5. The parameter values from the fitting cycle that gives the best fit for all cycles is shown here, along with the total fitting errors. Parameters fitted to individual cycles for every sample can be found in Appendix B.

Sample	$A$ (mm)	$E$ (kPa)	$\alpha_1$	$\tau_1$ (s)	$\alpha_2$	$\tau_2$ (s)	$\epsilon_{exp}^{tot}$ (%)	$\epsilon^{tot}$ (%)	$\epsilon_{max}^{tot}$ (%)
S50-00	0.358	14.77	0.927	1.00	0.116	123.18	1.38	0.36	6.75
S50-10	0.406	16.44	0.637	1.03	0.079	156.72	1.41	0.34	8.40
S50-20	0.403	20.46	0.315	1.65	0.044	139.70	1.69	0.18	7.52
S48-00	0.382	18.91	0.899	1.39	0.102	135.28	2.25	0.38	10.58
S48-10	0.355	17.98	0.380	1.27	0.070	131.88	0.93	0.22	4.48
S48-20	0.428	24.33	0.505	0.94	0.041	172.33	1.36	0.20	6.27

samples were tested in similar stretch ranges ( $\sim 1.3 - 2.3$ ). Plots of  $E$  and  $E_{inst}$  (defined in eq. (34)) versus Silicone oil content, for the fixed cross-linker mass fraction of 1/50, are shown in Figure 13(b). It can be seen that the two moduli approach each other with increasing oil content. The closer the values of  $E$  and  $E_{inst}$ , the lesser the allowance for rate stiffening in the expansion response<sup>9</sup>. A small increase in the equilibrium branch modulus  $E$  is seen with increasing oil content. Note that comparison of individual non-equilibrium branch parameters across samples needs to be done with caution as the fitting optimisation is not unique for a multiple branch nonlinear viscoelastic model. Furthermore, the fitted parameters across different loading cycles show variation for even a given sample (Appendix B). Nevertheless, for all samples, the single set of optimal parameters reported in Table 6 perform well across all loading rates as indicated by the low prediction errors. The fitted material parameters can be used to predict the material response for any given deformation by use of eqs. (25) and (26) along with initial conditions for the viscous deformation tensors. The constitutive model could also be coded as a user material subroutine in finite element programs that can be used with the fitted material parameters to solve boundary value problems.

## 8. Summary and conclusions

The VCCE technique extracts local nonlinear elastic properties in soft material samples by performing volume controlled expansion of a cavity through injection of an incompressible and immiscible fluid, combined with active monitoring of pressure inside the cavity. In this work, several enhancements have been introduced to the VCCE technique that extend its capability to measurement of local nonlinear viscoelastic properties of soft solids at low to medium stretch rates ( $10^{-2} - 1 \text{ s}^{-1}$ ). First, the accuracy of the pressure measurement is vastly improved by measuring the pressure through a pressure sensor, instead of through reaction forces measured by the mechanical testing machine. For fluid injection, the change from regular syringes to gas-tight syringes of smaller cross sectional area, results in significantly more precise volume control of the cavity. The most significant modification is the new cavity expansion protocol proposed here.

<sup>9</sup>Note that the decreasing value of the ratio  $E_{inst}/E$  with increasing Silicone oil content does not automatically imply that the rate dependence of material response is decreasing with increasing oil content, since the viscosity material parameters are not constant across samples. However, the low fitting errors in Table 2 confirm that the model is capturing the experimentally observed decrease in rate dependence with increasing oil content.

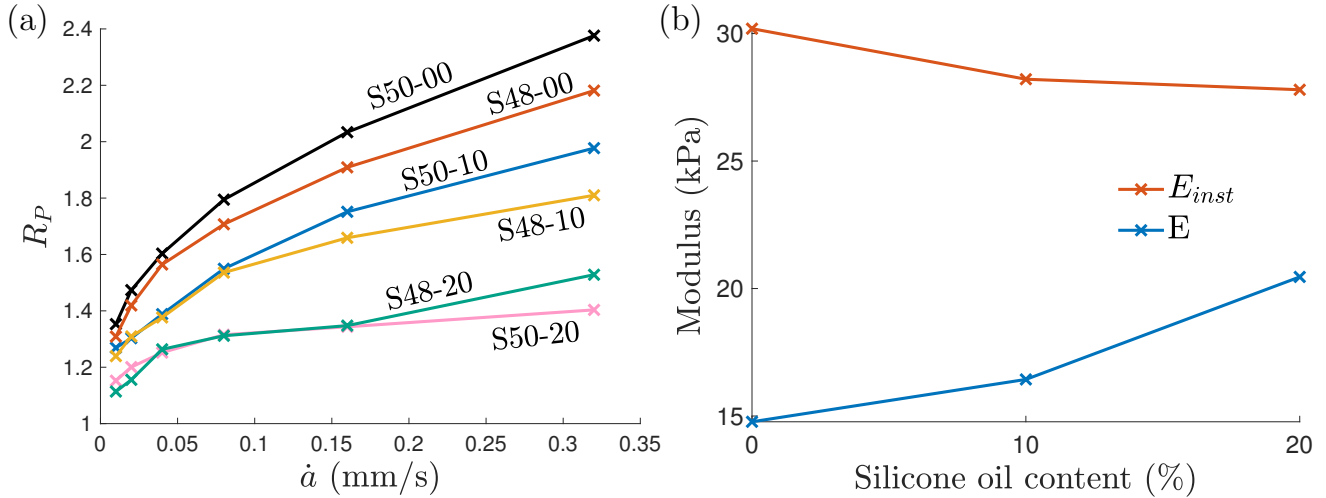


Figure 13: (a) Dynamic amplification ratio  $R_P$  increases with cavity expansion rates for all samples and decreases with increasing Silicone oil content for a given cross-linker mass fraction. (b) Plots of the modulus of equilibrium branch,  $E$ , and the instantaneous modulus,  $E_{inst} = E(1 + \alpha_1 + \alpha_2)$ , for fixed cross-linker mass fraction of 1/50. The two moduli approach each other with increasing Silicone oil content.

Instead of the constant volumetric expansion rate, conventionally used in VCCE and other needle based cavity expansion techniques, the new protocol specifies constant cavity stretch rate expansion that allows for observation of appreciable rate sensitivity. Accordingly, after eliminating the Mullins effect, several cycles of expansion-relaxation and retraction-recovery are performed at different expansion rates to capture the corresponding pressure response. Material parameters are determined by comparing the experimentally observed pressure profiles with theoretical predictions that are obtained using a generalized large deformation nonlinear viscoelastic model. It is shown that the equilibrium modulus can be directly inferred from the repeatable equilibrated pressures at two different cavity sizes, while the non-equilibrium parameters are determined by a best fit to the expansion-relaxation data.

Application of the technique to characterize the viscoelastic response of soft PDMS samples with tuneable content of Silicone oil, shows sensitivity and repeatability. The rate dependence of the material response is seen to reduce with increasing oil content for a given mass fraction of cross-linker. For the kinetic evolution law considered here, the fitted material parameters for all material compositions indicate two distinct timescales of relaxation, of the orders of  $\sim 1$  s and  $\sim 100$  s. Also, a single set of material parameters is shown to capture the pressure response across all the different cavity expansion rates with high accuracy.

Provided the measured viscoelastic properties of soft PDMS samples, obtained in this work, we set out to explain earlier reports of rate insensitivity exhibited in needle based cavity expansion methods. This investigation elucidates the significance of the specific expansion protocol and leads to a cautionary note on the quasistatic assumption in earlier work. It is found that even slow volumetric rate fluid injection can lead to high cavity stretch rates. These high stretch rates, which are more pronounced for smaller initial cavity size, can lead to viscoelastic stiffening that dominates the pressure response throughout the expansion, thus leading to an illusion of rate insensitivity. This effect can explain the higher reported values of the elastic modulus by cavity expansion/instability based studies in the literature, compared to conventional testing methods. The influence of viscoelastic stiffening of the material in explaining this discrepancy does not

seem to have been previously considered. Hence, the stretch rate controlled expansion protocol proposed in this paper becomes essential for accurate estimation of both quasistatic and dynamic material parameters.

This work is not without limitations. Additional advancements are needed to reliably apply this technique to more complex heterogeneous materials. Challenges might appear in isolation of a fracture free range and in interpretation of the pressure data. Additionally, the current approach assumes the material to be incompressible, and the specimen to be sufficiently large in comparison with the needle diameter. If these assumptions are relaxed, additional parameters should enter the theoretical prediction of the pressure response. Finally, this technique could potentially be extended, in the future, to characterise additional properties of soft materials. Fatigue that is observed across loading cycles in our experiments could perhaps be better characterised using a viscoplastic material model. Mullins effect is also captured here, for the first time in a spherically symmetric deformation setting. The VCCE technique can thus potentially aid in better characterization of this effect. Since the proposed technique can extract local nonlinear viscoelastic material properties in soft opaque materials while being minimally invasive, it should be a promising candidate for *in vivo* viscoelastic testing of biological tissues.

## Acknowledgements

The authors wish to acknowledge the support of: the Army Research Office, United States of America and Dr. Ralph A. Anthenien, Program Manager, under award number W911NF-19-1-0275; the Office of Naval Research, United States of America and Dr. Timothy B. Bentley, Program Manager, under award number N00014-20-1-2561; and helpful conversations with Aditya Kumar (University of Illinois at Urbana-Champaign), as well as the help from Seethalakshmi (Texas A&M University) in generation of figures.

## Appendix A. Viscoelastic modelling

### Appendix A.1. Constitutive model

Following the constitutive modelling approach in Kumar and Lopez-Pamies (2016); Kumar et al. (2017); Ghosh and Lopez-Pamies (2020), kinetic evolution laws for the viscous deformation  $\mathbf{F}_n^v$  are prescribed using dissipation potentials  $\phi_n(\mathbf{F}, \mathbf{F}_n^v, \dot{\mathbf{F}}_n^v)$  as

$$\frac{\partial \hat{\psi}_n}{\partial \mathbf{F}_n^v} (\mathbf{F} \mathbf{F}_n^{v-1}) + \frac{\partial \phi_n}{\partial \dot{\mathbf{F}}_n^v} (\mathbf{F}, \mathbf{F}_n^v, \dot{\mathbf{F}}_n^v) = 0 \quad \text{for } n = 1, 2, \dots, N \quad (\text{A.1})$$

The second law of thermodynamics, for isothermal processes, imposes the following constraint on the dissipation potentials

$$\sum_{n=1}^N \left[ \frac{\partial \phi_n}{\partial \dot{\mathbf{F}}_n^v} (\mathbf{F}, \mathbf{F}_n^v, \dot{\mathbf{F}}_n^v) \right] \cdot \dot{\mathbf{F}}_n^v \geq 0 \quad (\text{A.2})$$

for arbitrary deformation gradients  $\mathbf{F}$ ,  $\mathbf{F}_n^v$ , with equality holding only when  $\dot{\mathbf{F}}_n^v = \mathbf{0}$  (for  $n = 1, 2, \dots, N$ ). The inequality (A.2) is automatically enforced if following  $N$  inequalities are satisfied

$$\left[ \frac{\partial \phi_n}{\partial \dot{\mathbf{F}}_n^v} \left( \mathbf{F}, \mathbf{F}_n^v, \dot{\mathbf{F}}_n^v \right) \right] \cdot \dot{\mathbf{F}}_n^v \geq 0 \quad \text{for } n = 1, 2, \dots, N \quad (\text{A.3})$$

Extending the modelling approach in Ghosh and Lopez-Pamies (2020) to multiple non-equilibrium branches, we choose the following dissipation potentials that satisfy (A.3),

$$\phi_n \left( \mathbf{F}, \mathbf{F}_n^v, \dot{\mathbf{F}}_n^v \right) = \frac{1}{2} \dot{\mathbf{F}}_n^v \mathbf{F}_n^{v-1} \cdot \left[ \mathcal{A}_n \left( \dot{\mathbf{F}}_n^v \mathbf{F}_n^{v-1} \right) \right] \quad , \quad \mathcal{A}_n = 2\eta_{K_n}(I_{1n}^v)\mathcal{K} + 3\eta_J\mathcal{J} \quad (\text{A.4})$$

where  $I_{1n}^v = \text{tr}(\mathbf{C}_n^v)$ ,  $\mathcal{K}_{ijkl} = 1/2 [\delta_{ik}\delta_{jl} + \delta_{il}\delta_{jk} - 2/3 \delta_{ij}\delta_{kl}]$ ,  $\mathcal{J}_{ijkl} = 1/3 \delta_{ij}\delta_{kl}$  and  $\eta_J \rightarrow +\infty$ . We note that  $\mathcal{K}$  is the symmetric deviatoric projection tensor such that<sup>10</sup>  $\mathcal{K}\mathbf{X} = \text{symdev}(\mathbf{X})$  and  $\mathcal{J}$  is the spherical projection tensor such that  $\mathcal{J}\mathbf{X} = \frac{1}{3}\text{tr}(\mathbf{X})\mathbf{I}$ , for any second order tensor  $\mathbf{X}$ . We select the viscosity function  $\eta_{K_n}(I_{1n}^v)$  to be the following increasing function of deformation

$$\eta_{K_n}(I_{1n}^v) = \frac{1}{2}\eta_n I_{1n}^v \quad (\text{A.5})$$

where  $\eta_n > 0$ . Differentiating (A.4) with respect to  $\dot{\mathbf{F}}_n^v$ , we have

$$\frac{\partial \phi_n}{\partial \dot{\mathbf{F}}_n^v} = \left( \mathcal{A}_n \left( \dot{\mathbf{F}}_n^v \mathbf{F}_n^{v-1} \right) \right) \mathbf{F}_n^{v-T} \quad (\text{A.6})$$

Using (6), we can write

$$\frac{\partial \psi_n}{\partial \mathbf{F}_n^v} = -\mathbf{M}_n \mathbf{F}_n^{v-T} \quad \text{where} \quad \mathbf{M}_n = \mathbf{F}_n^{eT} \frac{\partial \hat{\psi}_n}{\partial \mathbf{F}_n^e} \quad (\text{A.7})$$

Then, by using eqs. (A.1), (A.6) and (A.7), we can write

$$\mathbf{M}_n = \mathcal{A}_n \left( \dot{\mathbf{F}}_n^v \mathbf{F}_n^{v-1} \right) \quad (\text{A.8})$$

where we recall  $\mathcal{A}_n = 2\eta_{K_n}(I_{1n}^v)\mathcal{K} + 3\eta_J\mathcal{J}$ . We have  $\eta_J \rightarrow \infty$  which forces  $\text{tr}(\dot{\mathbf{F}}_n^v \mathbf{F}_n^{v-1}) = 0$ , and then taking the deviatoric part<sup>11</sup> of the two sides of (A.8) gives us

$$\mathbf{M}_n - \frac{1}{3}\text{tr}(\mathbf{M}_n)\mathbf{I} = 2\eta_{K_n} \text{sym} \left( \dot{\mathbf{F}}_n^v \mathbf{F}_n^{v-1} \right) \quad (\text{A.9})$$

Pre-multiplying both sides of (A.9) by  $\mathbf{F}_n^{vT}$  and post-multiplying by  $\mathbf{F}_n^v$ , we get

$$\mathbf{F}_n^{vT} \mathbf{M}_n \mathbf{F}_n^v - \frac{1}{3}\text{tr}(\mathbf{M}_n)\mathbf{C}_n^v = 2\eta_{K_n} \text{sym} \left( \mathbf{F}_n^{vT} \dot{\mathbf{F}}_n^v \right) = \eta_{K_n} \dot{\mathbf{C}}_n^v \quad (\text{A.10})$$

<sup>10</sup> $\text{symdev}(\mathbf{X}) = \frac{1}{2} (\text{dev}(\mathbf{X}) + (\text{dev}(\mathbf{X}))^T)$  where  $\text{dev}(\mathbf{X}) = \mathbf{X} - \frac{1}{3}\text{tr}(\mathbf{X})\mathbf{I}$ .

<sup>11</sup>The product  $\eta_J \text{tr}(\dot{\mathbf{F}}_n^v \mathbf{F}_n^{v-1})$  can have a finite limit and thus we remove the spherical component from both sides of (A.8).

which along with (A.5) yields the evolution equation (9). For the free energy functions in (24), we get

$$\mathbf{M}_n = \frac{\alpha_n E}{3} \mathbf{C}_n^e \quad , \quad \text{tr}(\mathbf{M}_n) = \frac{\alpha_n E}{3} \mathbf{C} \cdot \mathbf{C}_n^{v-1} \quad (\text{A.11})$$

where  $\mathbf{C}_n^e = \mathbf{F}_n^{eT} \mathbf{F}_n^e$ , and we have used  $\text{tr}(\mathbf{C}_n^e) = \text{tr}(\mathbf{C} \mathbf{C}_n^{v-1}) = \mathbf{C} \cdot \mathbf{C}_n^{v-1}$ . Substituting (A.11) in (A.10) and using (A.5), we obtain the evolution equation (26).

### Appendix A.2. Spherically symmetric deformation

For a free energy function of the form in Equation (19), the expression for the Cauchy stress in (8) yields

$$\boldsymbol{\sigma} = \frac{\partial \hat{\psi}_0}{\partial \mathbf{F}} \mathbf{F}^T + \sum_{n=1}^N \frac{\partial \hat{\psi}_n}{\partial \mathbf{F}_n^e} \mathbf{F}_n^{eT} - p \mathbf{I} \quad (\text{A.12})$$

With the free energy density written in terms of the principal stretch components ( $\bar{\psi}_0(\lambda_r, \lambda_\theta, \lambda_\phi)$  and  $\bar{\psi}_n(\lambda_{rn}^e, \lambda_{\theta n}^e, \lambda_{\phi n}^e)$ ) for the spherically symmetric deformation, the principal stress difference resulting from (A.12) can be shown to be

$$\sigma_\theta - \sigma_r = \lambda_\theta \frac{\partial \bar{\psi}_0}{\partial \lambda_\theta} - \lambda_r \frac{\partial \bar{\psi}_0}{\partial \lambda_r} + \sum_{n=1}^N \left( \lambda_{\theta n}^e \frac{\partial \bar{\psi}_n}{\partial \lambda_{\theta n}^e} - \lambda_{rn}^e \frac{\partial \bar{\psi}_n}{\partial \lambda_{rn}^e} \right) \quad (\text{A.13a})$$

$$= \frac{\lambda}{2} \tilde{\psi}'(\lambda) + \sum_{n=1}^N \frac{\lambda_{\theta n}^e}{2} \tilde{\psi}'_n(\lambda_{\theta n}^e) \quad (\text{A.13b})$$

where  $\tilde{\psi}_0(\lambda) = \bar{\psi}_0(\lambda^{-2}, \lambda, \lambda)$  and  $\tilde{\psi}_n(\lambda_{\theta n}^e) = \bar{\psi}_n(\lambda_{\theta n}^{e-2}, \lambda_{\theta n}^e, \lambda_{\theta n}^e)$ . Using (A.13b) and recalling that  $\lambda_{\theta n}^e = \lambda / \lambda_n^v$  from (11), we arrive at eq. (21). For the spherically symmetric deformation, (A.10) can be used to write

$$\dot{\lambda}_n^v = 2\lambda_n^v \dot{\lambda}_n^v = \frac{\lambda_n^{v2}}{\eta_{K_n}} \left( M_{\theta n} - \frac{1}{3} (M_{rn} + M_{\theta n} + M_{\phi n}) \right) \quad (\text{A.14})$$

where  $M_{\theta n} = M_{\phi n} = \lambda_{\theta n}^e \frac{\partial \bar{\psi}_n}{\partial \lambda_{\theta n}^e}$  and  $M_{rn} = \lambda_{rn}^e \frac{\partial \bar{\psi}_n}{\partial \lambda_{rn}^e}$ . Simplifying (A.14), we get

$$\dot{\lambda}_n^v = \frac{\lambda_n^v}{6\eta_{K_n}} \left( \lambda_{\theta n}^e \frac{\partial \bar{\psi}_n}{\partial \lambda_{\theta n}^e} - \lambda_{rn}^e \frac{\partial \bar{\psi}_n}{\partial \lambda_{rn}^e} \right) = \frac{\lambda}{12\eta_{K_n}} \tilde{\psi}'_n(\lambda_{\theta n}^e) \quad (\text{A.15})$$

Using (A.5) and the relation  $\lambda_{\theta n}^e = \lambda / \lambda_n^v$  in (A.15) gives us (23). Substituting (28) in (A.15) and using the definition of  $\tau_n$  in (26), we arrive at eq. (29).

### Appendix A.3. Numerical integration

For the numerical integration, we choose to work with a fixed set of material points. The Lagrangian coordinate space  $R \in [A \ B]$  is nonuniformly discretized such that the density of material points is higher closer to the cavity wall. The circumferential stretch for any material point is given by

$$\lambda(R, t) = \left( 1 + \left( \frac{A}{R} \right)^3 (\lambda_a^3(t) - 1) \right)^{1/3} \quad (\text{A.16})$$

Given a prescribed cavity wall deformation  $\lambda_a(t)$ , we time integrate the evolution equation for the viscous stretch  $\lambda_n^v(R, t)$ , written in terms of  $\lambda(R, t)$ ,

$$\dot{\lambda}_n^v(R, t) = \frac{4}{3\tau_n} \frac{1}{(2\lambda_n^{v^2} + \lambda_n^{v^{-4}})} \left( \frac{\lambda^6 - \lambda_n^{v^6}}{\lambda_n^v \lambda^4} \right) \quad (\text{A.17})$$

The time integration is carried out using Matlab's 'ode45' method and the tolerance and initial step values are chosen so as to ensure convergence for even small values of the parameters  $\tau_n$ . Separate time integrations are done for the expansion-relaxation and retraction-recovery part of every loading cycle using the initial conditions described in Section 5.6. Using eqs. (14) and (15) and the integrated values for  $\lambda_n^v(R, t)$ , the integration in (27) is carried out using a trapezoidal rule to calculate the gauge pressure  $P(t)$ . For evaluation of the inertial pressure term  $P_{in}(t)$ , we take  $\rho = 965 \text{ kg/m}^3$  and  $\ddot{\lambda}_a = 0$ , but as noted earlier in Section 5.3,  $P_{in}(t)$  is insignificant compared to  $S(t)$ .

#### Appendix A.4. Parameter fitting

For every cycle, the equilibrated pressures at the start and end of the expansion-relaxation process,  $P_{s1}$  and  $P_{s2}$ , are used to fit for the parameters  $E$  and  $A$  as described in Section 6.1. To fit for the parameters  $\alpha_1, \alpha_2, \tau_1$  and  $\tau_2$  we make use of Matlab's nonlinear least squares method 'lsqnonlin' using the 'trust-region-reflective' algorithm. For the residual function, the pressure obtained from the numerical integration discussed in the previous section is subtracted from the experimental pressure data. First, control pressure profiles are generated by integrating the material model for given values of the viscoelastic parameters and it is ensured that the fitting method is able to exactly capture the chosen parameters. During this control testing, the convergence speed of the algorithm is optimised by experimenting with the scaling of the parameters using the 'TypicalX' argument of 'lsqnonlin'. The optimised fitting method is then used to fit the experimental data. It is also ensured that the fitting is roughly insensitive to the initial guess values for the parameters. The parameters are fitted for the expansion-relaxation part of the pressure profiles but the fitted parameters also predict the retraction-recovery profiles well. Since the expansion part of the loading cycle happens over a small fraction of the total time for expansion-relaxation, the pressure data is sampled non-uniformly for fitting so as to have a higher density of data points in the expansion part of the pressure-time curves. The fitting errors reported are, however, area integrals that are not affected by the re-sampling for fitting purposes. Also note that while using a single set of non-equilibrium parameters  $(\alpha_1, \alpha_2, \tau_1, \tau_2)$  to predict the pressure response for all the loading cycles, the parameter values for  $E$  and  $A$  are always taken to be the values fitted to the individual cycles.

## Appendix B. Fitted parameters for all cycles

Sample	Cycle	$A$ (mm)	$E$ (kPa)	$\alpha_1$	$\tau_1$ (s)	$\alpha_2$	$\tau_2$ (s)	$\epsilon_{exp}$ (%)	$\epsilon$ (%)	$\epsilon_{max}$ (%)
S50-00	1	0.353	14.71	0.597	2.76	0.097	154.63	0.23	0.18	1.45
S50-00	2	0.356	14.77	0.789	1.54	0.109	129.07	0.37	0.27	2.17
S50-00	3	0.358	14.77	0.927	1.00	0.116	123.18	0.47	0.36	2.67
S50-00	4	0.360	14.79	1.246	0.56	0.128	110.56	0.50	0.44	4.06
S50-00	5	0.363	14.83	1.599	0.32	0.140	97.16	0.63	0.53	5.87
S50-10	1	0.396	16.31	0.503	2.46	0.070	175.03	0.28	0.17	1.64
S50-10	2	0.398	16.27	0.468	2.06	0.076	182.61	0.43	0.22	2.07
S50-10	3	0.406	16.44	0.637	1.03	0.079	156.72	0.58	0.28	3.44
S50-10	4	0.412	16.53	0.697	0.74	0.083	135.58	0.75	0.35	6.98
S50-10	5	0.416	16.71	0.959	0.37	0.088	94.77	0.88	0.37	6.10
S50-20	1	0.402	20.43	0.309	2.44	0.040	148.00	0.46	0.11	1.56
S50-20	2	0.403	20.46	0.315	1.65	0.044	139.70	0.52	0.14	1.71
S50-20	3	0.404	20.48	0.404	0.85	0.051	125.91	0.79	0.18	3.17
S50-20	4	0.406	20.54	0.487	0.44	0.058	108.79	0.85	0.22	4.30
S50-20	5	0.408	20.64	0.262	0.67	0.053	112.77	0.94	0.23	2.91
S48-00	1	0.378	18.81	0.706	2.48	0.089	160.14	0.31	0.20	1.68
S48-00	2	0.382	18.91	0.899	1.39	0.102	135.28	0.40	0.29	2.16
S48-00	3	0.385	18.98	1.367	0.65	0.118	115.38	0.57	0.40	3.35
S48-00	4	0.390	19.12	1.684	0.36	0.138	88.20	0.75	0.49	4.62
S48-00	5	0.391	19.09	1.960	0.25	0.138	102.76	0.87	0.59	6.71
S48-10	1	0.348	17.89	0.135	9.34	0.052	179.11	0.37	0.08	1.38
S48-10	2	0.351	17.98	0.203	4.34	0.057	139.47	0.50	0.10	1.93
S48-10	3	0.349	17.84	0.273	2.56	0.066	169.41	0.66	0.16	2.56
S48-10	4	0.355	17.98	0.380	1.27	0.070	131.88	0.83	0.21	3.19
S48-10	5	0.357	18.03	0.644	0.49	0.077	112.00	0.81	0.29	3.04
S48-20	1	0.420	24.13	0.376	2.32	0.033	200.36	0.36	0.10	1.33
S48-20	2	0.424	24.22	0.440	1.47	0.039	178.49	0.55	0.13	2.32
S48-20	3	0.428	24.33	0.505	0.94	0.041	172.33	0.69	0.18	2.52
S48-20	4	0.433	24.47	0.517	0.74	0.039	186.29	0.81	0.23	2.77
S48-20	5	0.438	24.63	0.621	0.43	0.046	146.80	0.81	0.28	3.73

## References

Balooch, M., Wu-Magidi, I.-C., Balazs, A., Lundkvist, A., Marshall, S., Marshall, G., Siekhaus, W., Kinney, J., 1998. Viscoelastic properties of demineralized human dentin measured in water with atomic force microscope (afm)-based indentation. *Journal of Biomedical Materials Research: An Official Journal of The Society for Biomaterials, The Japanese Society for Biomaterials, and the Australian Society for Biomaterials* 40 (4), 539–544.

Blumlein, A., Williams, N., McManus, J. J., 2017. The mechanical properties of individual cell spheroids. *Scientific Reports* 7 (1), 1–10.

Budday, S., Nay, R., de Rooij, R., Steinmann, P., Wyrobek, T., Ovaert, T. C., Kuhl, E., 2015. Mechanical properties of gray and white matter brain tissue by indentation. *Journal of the mechanical behavior of biomedical materials* 46, 318–330.

Budday, S., Sommer, G., Holzapfel, G., Steinmann, P., Kuhl, E., 2017. Viscoelastic parameter identification of human brain tissue. *Journal of the mechanical behavior of biomedical materials* 74, 463–476.

Budday, S., Steinmann, P., Kuhl, E., 2014. The role of mechanics during brain development. *Journal of the Mechanics and Physics of Solids* 72, 75–92.

Castellanos, G., Arzt, E., Kamperman, M., 2011. Effect of viscoelasticity on adhesion of bioinspired micropatterned epoxy surfaces. *Langmuir* 27 (12), 7752–7759.

Chin, M. S., Freniere, B. B., Fakhouri, S., Harris, J. E., Lalikos, J. F., Crosby, A. J., 2013. Cavitation rheology as a potential method for in vivo assessment of skin biomechanics. *Plastic and reconstructive surgery* 131 (2), 303e.

Chockalingam, S., Cohen, T., 2020. Shear shock evolution in incompressible soft solids. *Journal of the Mechanics and Physics of Solids* 134, 103746.

Clément, F., Bokobza, L., Monnerie, L., 2001. On the mullins effect in silica-filled polydimethylsiloxane networks. *Rubber chemistry and technology* 74 (5), 847–870.

Cohen, T., Molinari, A., 2015. Dynamic cavitation and relaxation in incompressible nonlinear viscoelastic solids. *International Journal of Solids and Structures* 69, 544–552.

Crosby, A. J., McManus, J., 2011. Blowing bubbles to study living material. *Physics Today* 64 (2), 62–63.

Cui, J., Lee, C. H., Delbos, A., McManus, J. J., Crosby, A. J., 2011. Cavitation rheology of the eye lens. *Soft Matter* 7 (17), 7827–7831.

Delbos, A., Cui, J., Fakhouri, S., Crosby, A. J., 2012. Cavity growth in a triblock copolymer polymer gel. *Soft Matter* 8 (31), 8204–8208.

Diani, J., Fayolle, B., Gilormini, P., 2009. A review on the mullins effect. *European Polymer Journal* 45 (3), 601–612.

Engler, A. J., Griffin, M. A., Sen, S., Bonnemann, C. G., Sweeney, H. L., Discher, D. E., 2004. Myotubes differentiate optimally on substrates with tissue-like stiffness pathological implications for soft or stiff microenvironments. *Journal of Cell Biology* 166 (6), 877–887.

Estrada, J. B., Barajas, C., Henann, D. L., Johnsen, E., Franck, C., 2018. High strain-rate soft material characterization via inertial cavitation. *Journal of the Mechanics and Physics of Solids* 112, 291–317.

Finney, E., 1967. Dynamic elastic properties of some fruits during growth and development. *Journal of Agricultural Engineering Research* 12 (4), 249–256.

Fox, H., Taylor, P., Zisman, W., 1947. Polyorganosiloxanes... surface active properties. *Industrial & Engineering Chemistry* 39 (11), 1401–1409.

Fuentes-Caparrós, A. M., Dietrich, B., Thomson, L., Chauveau, C., Adams, D. J., 2019. Using cavitation rheology to understand dipeptide-based low molecular weight gels. *Soft matter* 15 (31), 6340–6347.

Ghosh, K., Lopez-Pamies, O., 2020. On the two-potential constitutive modeling of dielectric elastomers. *Meccanica*.

Hanson, D. E., Hawley, M., Houlton, R., Chitanvis, K., Rae, P., Orler, E. B., Wroblewski, D. A., 2005. Stress softening experiments in silica-filled polydimethylsiloxane provide insight into a mechanism for the mullins effect. *Polymer* 46 (24), 10989–10995.

Hu, Y., Zhao, X., Vlassak, J. J., Suo, Z., 2010. Using indentation to characterize the poroelasticity of gels. *Applied Physics Letters* 96 (12), 121904.

Huang, L., Yang, X., Gao, J., 2019. Pseudo-elastic analysis with permanent set in carbon-filled rubber. *Advances in Polymer Technology* 2019.

Ismail, A. E., Grest, G. S., Heine, D. R., Stevens, M. J., Tsige, M., 2009. Interfacial structure and dynamics of siloxane systems: Pdms- vapor and pdms- water. *Macromolecules* 42 (8), 3186–3194.

Kong, H. J., Liu, J., Riddle, K., Matsumoto, T., Leach, K., Mooney, D. J., 2005. Non-viral gene delivery regulated by stiffness of cell adhesion substrates. *Nature materials* 4 (6), 460–464.

Kumar, A., Aranda-Iglesias, D., Lopez-Pamies, O., 2017. Some remarks on the effects of inertia and viscous dissipation in the onset of cavitation in rubber. *Journal of Elasticity* 126 (2), 201–213.

Kumar, A., Lopez-Pamies, O., 2016. On the two-potential constitutive modeling of rubber viscoelastic materials. *Comptes Rendus Mecanique* 344 (2), 102–112.

Last, J. A., Pan, T., Ding, Y., Reilly, C. M., Keller, K., Acott, T. S., Fautsch, M. P., Murphy, C. J., Russell, P., 2011. Elastic modulus determination of normal and glaucomatous human trabecular meshwork. *Investigative ophthalmology & visual science* 52 (5), 2147–2152.

Lin, D. C., Shreiber, D. I., Dimitriadis, E. K., Horkay, F., 2009. Spherical indentation of soft matter beyond the hertzian regime: numerical and experimental validation of hyperelastic models. *Biomechanics and modeling in mechanobiology* 8 (5), 345.

Liu, F., Li, C., Liu, S., Genin, G. M., Huang, G., Lu, T., Xu, F., 2015. Effect of viscoelasticity on skin pain sensation. *Theoretical and Applied Mechanics Letters* 5 (6), 222–226.

Mahaffy, R., Park, S., Gerde, E., Käs, J., Shih, C., 2004. Quantitative analysis of the viscoelastic properties of thin regions of fibroblasts using atomic force microscopy. *Biophysical journal* 86 (3), 1777–1793.

Mao, Y., Lin, S., Zhao, X., Anand, L., 2017. A large deformation viscoelastic model for double-network hydrogels. *Journal of the Mechanics and Physics of Solids* 100, 103–130.

Mijailovic, A. S., Galarza, S., Raayai-Ardakani, S., Birch, N. P., Schiffman, J. D., Crosby, A. J., Cohen, T., Peyton, S. R., J. Van Vliet, K., 2020. Localized measurement of brain tissue mechanical properties by needle induced cavitation rheology and volume controlled cavity expansion.

Mishra, S., Lacy, T. E., Kundu, S., 2018. Effect of surface tension and geometry on cavitation in soft solids. *International Journal of Non-Linear Mechanics* 98, 23–31.

Nickerson, C. S., Park, J., Kornfield, J. A., Karageozian, H., 2008. Rheological properties of the vitreous and the role of hyaluronic acid. *Journal of biomechanics* 41 (9), 1840–1846.

Paszek, M. J., Zahir, N., Johnson, K. R., Lakins, J. N., Rozenberg, G. I., Gefen, A., Reinhart-King, C. A., Margulies, S. S., Dembo, M., Boettiger, D., et al., 2005. Tensional homeostasis and the malignant phenotype. *Cancer cell* 8 (3), 241–254.

Polio, S. R., Kundu, A. N., Dougan, C. E., Birch, N. P., Aurian-Blajeni, D. E., Schiffman, J. D., Crosby, A. J., Peyton, S. R., 2018. Cross-platform mechanical characterization of lung tissue. *PloS one* 13 (10), e0204765.

Prowse, M. S., Wilkinson, M., Puthoff, J. B., Mayer, G., Autumn, K., 2011. Effects of humidity on the mechanical properties of gecko setae. *Acta biomaterialia* 7 (2), 733–738.

Raayai-Ardakani, S., Chen, Z., Earl, D. R., Cohen, T., 2019a. Volume-controlled cavity expansion for probing of local elastic properties in soft materials. *Soft matter* 15 (3), 381–392.

Raayai-Ardakani, S., Cohen, T., 2019. Capturing strain stiffening using volume controlled cavity expansion. *Extreme Mechanics Letters* 31, 100536.

Raayai-Ardakani, S., Earl, D. R., Cohen, T., 2019b. The intimate relationship between cavitation and fracture. *Soft matter* 15 (25), 4999–5005.

Rashid, B., Destrade, M., Gilchrist, M. D., 2012. Inhomogeneous deformation of brain tissue during tension tests. *Computational Materials Science* 64, 295–300.

Reza, A., Shishesaz, M., Naderan-Tahan, K., 2014. The effect of viscoelasticity on creep behavior of double-lap adhesively bonded joints. *Latin American Journal of Solids and Structures* 11 (1), 35–50.

Samani, A., Plewes, D., 2007. An inverse problem solution for measuring the elastic modulus of intact *ex vivo* breast tissue tumours. *Physics in Medicine & Biology* 52 (5), 1247.

Solomon, W., Jindal, V., 2007. Modeling changes in rheological properties of potatoes during storage under constant and variable conditions. *LWT-Food Science and Technology* 40 (1), 170–178.

Streitberger, K.-J., Wiener, E., Hoffmann, J., Freimann, F. B., Klatt, D., Braun, J., Lin, K., McLaughlin, J., Sprung, C., Klingebiel, R., et al., 2011. *In vivo* viscoelastic properties of the brain in normal pressure hydrocephalus. *NMR in Biomedicine* 24 (4), 385–392.

Style, R. W., Hyland, C., Boltyanskiy, R., Wettlaufer, J. S., Dufresne, E. R., 2013. Surface tension and contact with soft elastic solids. *Nature communications* 4 (1), 1–6.

Tram, N. K., Swindle-Reilly, K. E., 2018. Rheological properties and age-related changes of the human vitreous humor. *Frontiers in bioengineering and biotechnology* 6, 199.

VanLandingham, M. R., Chang, N.-K., Drzal, P., White, C. C., Chang, S.-H., 2005. Viscoelastic characterization of polymers using instrumented indentation. i. quasi-static testing. *Journal of Polymer Science Part B: Polymer Physics* 43 (14), 1794–1811.

Vedadghavami, A., Minooei, F., Mohammadi, M. H., Khetani, S., Kolahchi, A. R., Mashayekhan, S., Sanati-Nezhad, A., 2017. Manufacturing of hydrogel biomaterials with controlled mechanical properties for tissue engineering applications. *Acta biomaterialia* 62, 42–63.

von Streng, V., Abi-Akl, R., Giovanardi, B., Cohen, T., 2020. Morphogenesis and proportionate growth: A finite element investigation of surface growth with coupled diffusion. *arXiv preprint arXiv:2005.10747*.

Yang, J., Cramer III, H. C., Franck, C., 2020. Extracting non-linear viscoelastic material properties from violently-collapsing cavitation bubbles. *Extreme Mechanics Letters*, 100839.

Yang, S., Bahk, D., Kim, J., Kataruka, A., Dunn, A. C., Hutchens, S. B., 2019. Hydraulic fracture geometry in ultrasoft polymer networks. *International Journal of Fracture* 219 (1), 89–99.

Yeh, W.-C., Li, P.-C., Jeng, Y.-M., Hsu, H.-C., Kuo, P.-L., Li, M.-L., Yang, P.-M., Lee, P. H., 2002. Elastic modulus measurements of human liver and correlation with pathology. *Ultrasound in medicine & biology* 28 (4), 467–474.

Zheng, Y. P., Mak, A. F. T., 06 1999. Extraction of Quasi-Linear Viscoelastic Parameters for Lower Limb Soft Tissues From Manual Indentation Experiment. *Journal of Biomechanical Engineering* 121 (3), 330–339.

Zilonova, E., Solovchuk, M., Sheu, T., 2018. Bubble dynamics in viscoelastic soft tissue in high-intensity focal ultrasound thermal therapy. *Ultrasonics Sonochemistry* 40, 900–911.

Zimberlin, J. A., Crosby, A. J., 2010. Water cavitation of hydrogels. *Journal of Polymer Science Part B: Polymer Physics* 48 (13), 1423–1427.

Zimberlin, J. A., McManus, J. J., Crosby, A. J., 2010. Cavitation rheology of the vitreous: mechanical properties of biological tissue. *Soft Matter* 6 (15), 3632–3635.

Zimberlin, J. A., Sanabria-DeLong, N., Tew, G. N., Crosby, A. J., 2007. Cavitation rheology for soft materials. *Soft Matter* 3 (6), 763–767.